



Universiteit
Leiden
The Netherlands

Regulation of actomyosin contraction as a driving force of invasive lobular breast cancer

Schipper, K.

Citation

Schipper, K. (2020, December 3). *Regulation of actomyosin contraction as a driving force of invasive lobular breast cancer*. Retrieved from <https://hdl.handle.net/1887/138484>

Version: Publisher's Version

License: [Licence agreement concerning inclusion of doctoral thesis in the Institutional Repository of the University of Leiden](#)

Downloaded from: <https://hdl.handle.net/1887/138484>

Note: To cite this publication please use the final published version (if applicable).

Cover Page



Universiteit Leiden



The handle <http://hdl.handle.net/1887/138484> holds various files of this Leiden University dissertation.

Author: Schipper, K.

Title: Regulation of actomyosin contraction as a driving force of invasive lobular breast cancer

Issue date: 2020-12-03

Transcriptomics and Transposon Mutagenesis Identify Multiple Mechanisms of Resistance to the FGFR Inhibitor AZD4547

5

Sjors M. Kas^{1,10,*}, Julian R. de Ruiter^{1,2,10,*}, Koen Schipper^{1,10}, Eva Schut^{1,10}, Lorenzo Bombardelli^{3,10}, Ellen Wientjens^{1,10}, Anne Paulien Drenth^{1,10}, Renske de Korte-Grimmerink^{1,10}, Sunny Mahakena⁴, Christopher Phillips⁵, Paul D. Smith⁶, Sjoerd Klarenbeek⁷, Koen van de Wetering^{4,8}, Anton Berns^{3,10}, Lodewyk F.A. Wessels^{2,9,10}, Jos Jonkers^{1,10}

1. Division of Molecular Pathology, The Netherlands Cancer Institute, Amsterdam, The Netherlands.
 2. Division of Molecular Carcinogenesis, The Netherlands Cancer Institute, Amsterdam, The Netherlands.
 3. Division of Molecular Genetics, The Netherlands Cancer Institute, Amsterdam, The Netherlands.
 4. Division of Molecular Oncology, The Netherlands Cancer Institute, Amsterdam, The Netherlands.
 5. Discovery Sciences, IMED Biotech Unit, AstraZeneca, Cambridge, UK.
 6. Bioscience, Oncology, IMED Biotech Unit, AstraZeneca, Cambridge, UK.
 7. Experimental Animal Pathology, The Netherlands Cancer Institute, Amsterdam, The Netherlands.
 8. Present address: Department of Dermatology & Cutaneous Biology, Sidney Kimmel Medical College, Philadelphia, USA.
 9. Department of EEMCS, Delft University of Technology, Delft, The Netherlands.
 10. OncoCode Institute, Amsterdam, The Netherlands.
- * These authors contributed equally to this work

Abstract

In human cancers, fibroblast growth factor receptor (FGFR) signaling is frequently hyperactivated by deregulation of FGF ligands or by activating mutations in the FGFR receptors such as gene amplifications, point mutations and gene fusions. As such, FGFR inhibitors are considered an attractive therapeutic strategy for patients with mutations in FGFR family members. We previously identified *Fgfr2* as a key driver of invasive lobular carcinoma (ILC) in an *in vivo* insertional mutagenesis screen using the *Sleeping Beauty* (SB) transposon system. Here we explore whether these FGFR-driven ILCs are sensitive to the FGFR inhibitor AZD4547 and use transposon mutagenesis in these tumors to identify potential mechanisms of resistance to therapy. Combined with RNA sequencing-based analyses of AZD4547-resistant tumors, our *in vivo* approach identified several known and novel potential resistance mechanisms to FGFR inhibition, most of which converged on reactivation of the canonical MAPK-ERK signaling cascade. Observed resistance mechanisms included mutations in the tyrosine kinase domain of FGFR2, overexpression of MET, inactivation of RASA1, and activation of the drug-efflux transporter ABCG2. ABCG2 and RASA1 were identified only from *de novo* transposon insertions acquired during AZD4547 treatment, demonstrating that insertional mutagenesis in mice is an effective tool for identifying potential mechanisms of resistance to targeted cancer therapies.

Introduction

Fibroblast growth factor receptors (FGFRs) are members of the receptor tyrosine kinase (RTK) family that bind to different fibroblast growth factor (FGF) family members and are upstream of both the MAPK-ERK and PI3K-AKT signaling pathways. FGFRs dimerize upon FGF ligand binding, which results in cross-phosphorylation of the receptors cognate kinase domains and allows the binding of the adaptor protein FGFR substrate 2 α (FRS2 α), a key transducer of FGFR signaling¹. Once bound, subsequent phosphorylation of FRS2 α induces the recruitment of growth factor receptor-bound 2 (GRB2) and son of sevenless (SOS), resulting in activation of the MAPK-ERK signaling pathway. In contrast, activation of the PI3K-AKT signaling pathway is mediated by interactions between the FRS2 α complex and GRB2-associated binding protein 1 (GAB1)¹.

In human cancers, FGFR signaling is frequently hyper-activated by deregulation of FGF ligands or by activating mutations in the receptors, which predominantly consist of gene amplifications, point mutations and gene fusions^{2,3}. As such, FGFR inhibitors are considered to be an attractive therapeutic strategy for patients with mutations in FGFR family members. Currently, no FGFR-targeted therapies are approved for the treatment of human cancer, but multiple therapeutics targeting FGFR signaling are under investigation in several phase I/II clinical trials in different types of cancer^{2,3}. These encompass several different approaches for inhibiting FGFR, including non-selective and selective FGFR small-molecule tyrosine kinase inhibitors, monoclonal antibodies against FGFRs and FGF ligand traps.

Although these initial trials have shown promising results concerning tolerability and anti-tumor activity of several FGFR inhibitors in a subset of patients^{2,4-9}, more research is required to determine the right criteria for patient selection and to tackle potential resistance mechanisms to improve FGFR-targeted therapies. Several studies have already identified resistance mechanisms to FGFR-targeting agents, including polyclonal secondary FGFR mutations (including gatekeeper mutations)¹⁰⁻¹², activation of alternative RTKs¹³⁻¹⁶, and paracrine signaling of the tumor stroma^{17,18}. However, since most of these mechanisms are identified in *in vitro* studies, they may not encompass the complete spectrum of resistance mechanisms to FGFR inhibitors.

In a previous study, we identified *Fgfr2* as a key driver of invasive lobular breast carcinoma (ILC) using a *Sleeping Beauty* (SB)-based transposon insertional mutagenesis screen in mice¹⁹. In this work, we explore how mouse ILCs (mILCs) with SB transposon insertions in *Fgfr2* respond to treatment with the selective FGFR inhibitor AZD4547, and by which mechanisms they acquire resistance to FGFR inhibition. Our results show that the tumors exhibit increased FGFR signaling and initially regress upon treatment with AZD4547, but eventually develop treatment resistance. By performing a multi-omics analysis focusing on the resistant tumors, we identify several known and novel mechanisms by which tumors become resistant to AZD4547 treatment. Two of these mechanisms were uniquely identified from *de novo* transposon insertions that were acquired during treatment, demonstrating that insertional mutagenesis in mice is an effective tool for identifying resistance mechanisms to targeted cancer therapies.

Materials and methods

Orthotopic transplantations and AZD4547 intervention

Orthotopic transplantations of small tumor fragments were performed as previously described by Doornebal *et al.*²⁰. For the WESB-*Fgfr2* tumor-derived cells, 200.000 cells were injected orthotopically into the right fat pad of 8-15-week-old wild-type syngeneic recipient females in 20 μ l Matrigel (Corning) and PBS (1:1). For the WESB-*Fgfr2*-EV and WESB-*Fgfr2*-ABCG2 cells, 200.000 cells were injected orthotopically into the right fat pad of 8-week-old NMRI-nude females (Janvier Labs) in 20 μ l Matrigel (Corning) and PBS (1:1). All the drug interventions were initiated as soon as the mammary tumors reached a size of 5x5 mm (62.5 mm³; tumor volume: length x width² x 0.5). The treatments were performed daily by oral gavage for the indicated time with either the vehicle (1%-Tween-80 in demineralized water) or AZD4547 (AstraZeneca) at a dose of 12.5 mg/kg/day. The experimental cohort was monitored and mice were sacrificed (overall survival) when the (total) mammary tumor burden reached a size of approximately 1500 mm³ (tumor volume: length x width² x 0.5) or suffered from clinical signs of distress (respiratory distress, ascites, distended abdomen, rapid weight loss and severe anemia) caused by mammary tumor burden or metastatic disease. One hour after the last dosing, mice were sacrificed and the tumor, lungs, liver, spleen and tumor-draining lymph nodes were collected for further analysis. The mouse technicians were blinded to the sample groups for the treatments of WESB-*Fgfr2* and WESB-*Fgfr2*-ABCG2 established tumors in mice. All animal experiments were approved by the Animal Ethics Committee of the Netherlands Cancer Institute and performed in accordance with institutional, national and European guidelines for Animal Care and Use.

Cell culture

The isolation of primary tumor cells of the *SB*-induced mILCs (referred to as WESB cells) was performed as previously described by Kas *et al.*¹⁹. WESB cells were cultured in DMEM-F12 medium containing 10% fetal bovine serum (FBS), 100 IU/mL penicillin, 100 μ g/mL streptomycin (all from Life Technologies). MEF3.8 cells were cultured in DMEM-F12 medium containing 10% fetal bovine serum (FBS), 100 IU/mL penicillin, 100 μ g/mL streptomycin (all from Life Technologies). Phoenix packaging cells were cultured in Iscove's medium (Life Technologies) containing 10% FBS,

100 IU/ml penicillin, and 100 µg/ml streptomycin. WESB-*Fgfr2* cells were transduced with LZRS-IRES-GFP or LZRS-*Bcrp1*-IRES-GFP as previously described by Allen *et al.*²¹. Single GFP+ cells were sorted and allowed to recover before they were used in the experiments. Cell authentication was not conducted. All cell lines were kept at low passage and routinely tested for Mycoplasma contamination using the MycoAlert mycoplasma detection kit (Lonza).

Additional experimental details regarding the cell viability, clonogenic and competition assays are described in the Supplementary Data.

Vesicular Transport Assays

Vesicular transport assays were performed using the rapid filtration method as previously described^{22,23}. Additional experimental details are described in the Supplementary Data.

Nucleic acid isolation

DNA and RNA were isolated from whole tumor pieces using the Allprep DNA/RNA mini kit (Qiagen) according to the manufacturer's protocol.

Additional experimental details regarding the detection of the endogenous *Fgfr2-Tbc1d1* fusion and the *Met* qPCR copy number analysis are described in the Supplementary Data.

Analysis of SB transposon insertions

Transposon insertions were amplified and mapped following a previously described tagmentation-based DNA sequencing protocol²⁴. Additional experimental details and the analysis of the insertions sites are described in the Supplementary Data.

Antibodies

The primary antibodies to the following proteins were used: FGFR2 (1:1000, GeneTex 10648), phospho-FGFR (1:1000, CST 3471), FRS2 (1:1000, ProteinTech 11503-1-AP), phospho-FRS2 (Tyr436) (1:1000, Abcam 193363), AKT1 (1:1000, CST 2938), phospho-AKT(Ser473) (1:1000, CST 4060), p44/42 MAP kinase (1:1000, CST 4695), phospho-p44/42 MAPK ERK1/ERK2 (Thr202/Tyr204) (1:1000 CST 9101), ABCG2 (1:400, Abcam 24115) and

β -actin (1:50000, Sigma A5441).

Additional details regarding immunoblotting and immunohistochemistry are described in the Supplementary Data.

***In silico* modelling of the FGFR2 kinase in complex with the inhibitor AZD4547**

A composite complex of AZD4547 bound to mutated FGFR2 was built using the crystal structure of the FGFR1 kinase domain in complex with AZD4547 (PDB code V405) as a template. A structural alignment of the FGFR2 kinase domain crystal structure (PDB code 2PVF) was performed and the positions of the resistance mutations were mapped onto this alignment. Molecular graphic images were prepared using the CHIMERA package²⁵.

Statistical analysis

For the mouse studies, no statistical tests were performed to determine the appropriate sample size. Survival probabilities were estimated using the Kaplan–Meier method and compared using the Mantel–Cox test. The effect of AZD4547 treatment on tumor growth of WESB-*Fgfr2*-EV and WESB-*Fgfr2*-ABCG2 established tumors was tested using mixed linear models (details in Supplementary Data). To test for differential expression of *Abcg2*, *Rasa1* and *Pcdh15* over the insertion sites across all *SB*-induced tumors, we used the group-wise differential expression test implemented in IM-Fusion²⁶. The investigators were not blinded to the sample groups for all experiments. Graphs and error bars represent means \pm s.d. Python 3.5, R 3.3.1 and GraphPad Prism 7.03 were used for the statistical analyses. *P* values < 0.05 were considered significant.

Data availability

Raw tagmentation and RNA-sequencing data are available in ENA under accession number PRJEB25507.

Results

Activation of *Fgfr2* induces mouse ILC formation

In a previous study, we performed a *Sleeping Beauty* (*SB*) insertional

mutagenesis screen in mice with mammary-specific inactivation of *Cdh1* (encoding E-cadherin) to identify genes and pathways driving the development of invasive lobular breast carcinoma (ILC)¹⁹. Analysis of common insertion sites (CISs) in the *SB*-induced mouse ILCs (mILCs) showed that a majority (56 out of 99) of these tumors had *SB* insertions in *Fgfr2*, providing strong evidence that *Fgfr2* is a driver of ILC.

To confirm active FGFR signaling in mILCs with *SB* insertions in *Fgfr2*, we established cell lines from two *SB*-induced tumors, one with an insertion upstream of *Fgfr2* (WESB-*Fgfr2*) and one without an insertion in or near *Fgfr2* (WESB). We next compared the expression of FGFR2 and downstream signaling proteins between the two tumor cell lines. Although immunoblot analysis with an anti-FGFR2 antibody revealed no expression of native FGFR2 in either of the cell lines, we observed a doublet of approximately 240 kDa that was only expressed in the WESB-*Fgfr2* cell line (Fig. 1a). This size coincided with the predicted protein size of a gene fusion between *Fgfr2* and *Tbc1d1* (Supplementary Fig. 1a, 1b), which we previously identified in RNAseq data from this *SB*-induced mILC²⁶. Similar FGFR2 gene fusions were previously identified in several other studies, which demonstrated that these fusions result in increased FGFR signaling²⁷. In line with this, comparison of signaling proteins downstream of FGFR2 showed increased expression of phosphorylated FRS2α in WESB-*Fgfr2* tumor-derived cells compared to WESB cells.

These results demonstrate that WESB-*Fgfr2* cells show increased expression of an *Fgfr2-Tbc1d1* fusion gene, which is driven by an *SB* insertion upstream of *Fgfr2*. The increased expression of this fusion gene results in activation of FGFR signaling, suggesting that FGFR inhibition could be an interesting therapeutic strategy in these tumors.

Mouse ILCs with *SB* insertions in *Fgfr2* are dependent on FGFR signaling

To determine if WESB-*Fgfr2* cells were indeed sensitive to FGFR inhibition, we treated these cells with the selective FGFR inhibitor AZD4547, which is currently being evaluated in several early phase clinical trials². After treatment with 100 nM AZD4547, WESB-*Fgfr2* cells showed a decrease in expression of phosphorylated FGFR, FRS2α and ERK1/2 (Fig. 1b), confirming inhibition of the FGFR signaling pathway. Compared to WESB cells, the WESB-*Fgfr2* cells also showed reduced viability upon exposure to increasing concentrations of AZD4547 (Supplementary Fig. 1c), indicating

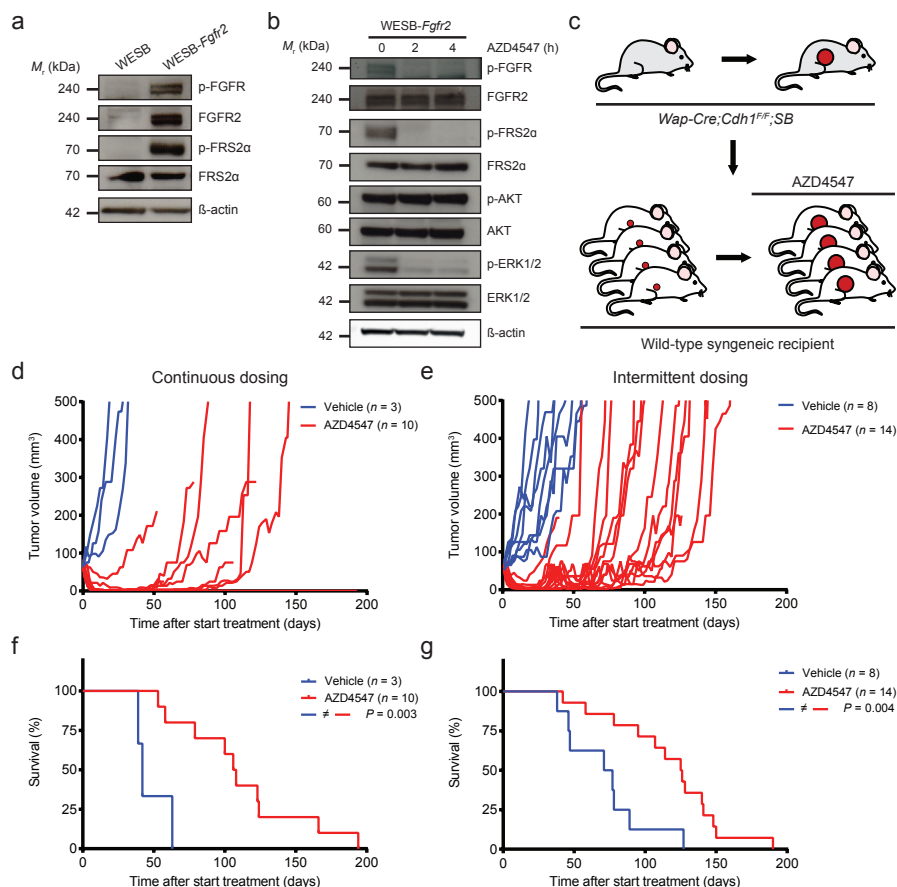


Figure 1: Intervention study with AZD4547 in mILCs with active FGFR signaling (a) Representative immunoblot ($n = 3$) for the expression of FGFR2 and its downstream signaling proteins in WESB and WESB-*Fgfr2* cells. β -Actin was used as a loading control. (b) The effect of FGFR inhibition on FGFR signaling in WESB-*Fgfr2* cells after short-term treatment with the FGFR inhibitor AZD4547 (100 nmol/L), as visualized by immunoblotting with antibodies detecting total and phosphorylated FGFR, FRS2 α , AKT, and ERK1/2. β -Actin was used as a loading control. (c) Schematic overview depicting the orthotopic transplantation of SB-induced mILC fragments into wild-type syngeneic recipient mice and the subsequent drug intervention with AZD4547. D and E, Tumor growth kinetics of orthotopically transplanted WESB-*Fgfr2* tumors under the continuous (d) and intermittent (e) treatment schedules with vehicle (blue) or AZD4547 (red). (f, g) Kaplan-Meier curves showing the overall survival of tumor-bearing mice under continuous (f) and intermittent (g) treatment with vehicle (blue) or AZD4547 (red). P values were calculated using a Mantel-Cox test.

that WESB-*Fgfr2* cells are dependent on FGFR signaling for their survival *in vitro*.

To determine the efficacy of AZD4547 *in vivo*, we orthotopically transplanted WESB-*Fgfr2* tumor fragments into multiple wild-type syngeneic recipient

animals and treated these animals with vehicle or AZD4547 (12.5 mg/kg/day) daily via oral gavage (Fig. 1c). To reduce the potential toxicity of prolonged treatment and to test the effect of a “drug holiday” on tumor growth, the animals were treated using either a continuous or an intermittent dosing schedule (Supplementary Fig. 1d). In both dosing schedules, tumors treated with AZD4547 showed decreased expression of downstream FGFR signaling and increased expression of cleaved caspase-3 (Supplementary Fig. 1e-g), which resulted in tumor regression within 10-20 days after start of the treatment (Fig. 1d, 1e). Furthermore, the majority of the AZD4547-treated tumors (9 out of 10 continuous-treated and 13 out of 14 intermittent-treated tumors) did not show any regrowth within the first treatment cycle of 24 days.

In the majority of mice, continuous treatment with AZD4547 resulted in tumor control for at least 40 days after start of the treatment, resulting in an increased overall survival compared to the vehicle-treated animals (Fig. 1f). Notably, 2 out of 10 sacrificed animals did not show any remaining tumor cells. In contrast, all intermittently treated mice showed tumor regrowth after the first treatment cycle of 24 days. However, these tumors remained sensitive to multiple additional cycles of AZD4547 treatment (Supplementary Fig. 2a), resulting in an increased overall survival compared to the vehicle-treated animals (Fig. 1g). Similar results were obtained with continuous AZD4547 treatment of mice after the orthotopic injection of WESB-*Fgfr2* tumor-derived cells (Supplementary Fig. 2b, 2c).

While the overall survival of AZD4547-treated mice was increased compared to vehicle-treated animals, there was no significant difference in survival between the continuous dosing (107 days) and the intermittent dosing (126 days) groups. However, in the continuous dosing group an increased number of animals succumbed due to clinical signs of distress (respiratory distress, ascites, distended abdomen, rapid weight loss and severe anemia), suggesting that the intermittent treatment schedule is less toxic for the animals (Supplementary Fig. 2d). In spite of the potent anti-cancer activity of AZD4547, both treatment schedules failed to deliver long-term tumor control, most likely due to the emergence of acquired therapy resistance. This reflects the major problem observed in cancer patients treated with targeted anti-cancer therapies.

Transcriptome analysis identifies known and novel secondary FGFR2 mutations and increased MET expression in AZD4547-resistant tumors

To explore potential resistance mechanisms to FGFR inhibition, we performed RNA-sequencing of AZD4547-sensitive and -resistant tumors obtained from vehicle-treated and AZD4547-treated animals (Supplementary Table S1), respectively, and compared their mutational spectra to identify mutations that were acquired during AZD4547 treatment. In this approach, we initially focused on known resistance mechanisms to FGFR-targeting therapeutics^{10–16}, which include upregulation of alternative RTKs and secondary FGFR mutations.

To assess if upregulation of other RTKs could explain the resistance of these tumors, we used RNA-sequencing data to determine changes in gene expression for *Kit*, *Met*, and all FGFR-, EGFR- and IGF-related RTKs. For this purpose, we employed DIDS, an algorithm that is specifically designed to identify differentially expressed genes in heterogeneous populations²⁸. Although this analysis did not identify any RTKs that were significantly differentially expressed across multiple samples, it did identify two AZD4547-resistant tumors with increased expression of *Met* (also known as hepatocyte growth factor receptor (HGFR)) and one AZD4547-resistant tumor with increased expression of insulin like growth factor 1 receptor (*Igf1r*), compared to vehicle-treated tumors (Fig. 2a, Supplementary Fig. 3a). Subsequent analysis of IGF1R and MET protein expression by immunohistochemistry (IHC) did not support IGF1R as a potential resistance mechanism, since no correlation was observed between expression levels of *Igf1r* mRNA and IGF1R protein (Fig. 2b). In contrast, both AZD4547-resistant tumors with high *Met* mRNA expression showed amplification of *Met* (Supplementary Fig. 3b) and over-expression of MET protein (Fig. 2c), whereas vehicle-, AZD4547-treated and other AZD4547-resistant tumors were negative for MET expression (Supplementary Fig. 3c). These *in vivo* results are in line with previous *in vitro* studies showing that upregulation of MET attenuates the efficacy of FGFR inhibition in tumor cells^{14,15}, indicating that upregulation of MET may also counteract the therapeutic efficacy of AZD4547 *in vivo*. In contrast to previous *in vitro* studies^{13,16}, we did not observe an obvious increase in mRNA expression of the epidermal growth factor receptor (*Egfr*) or other EGFR-family members in any of the AZD4547-resistant tumors.

Next, to determine if any mutations in RTKs or members of the MAPK-ERK pathway could explain the resistance of these tumors, we used the

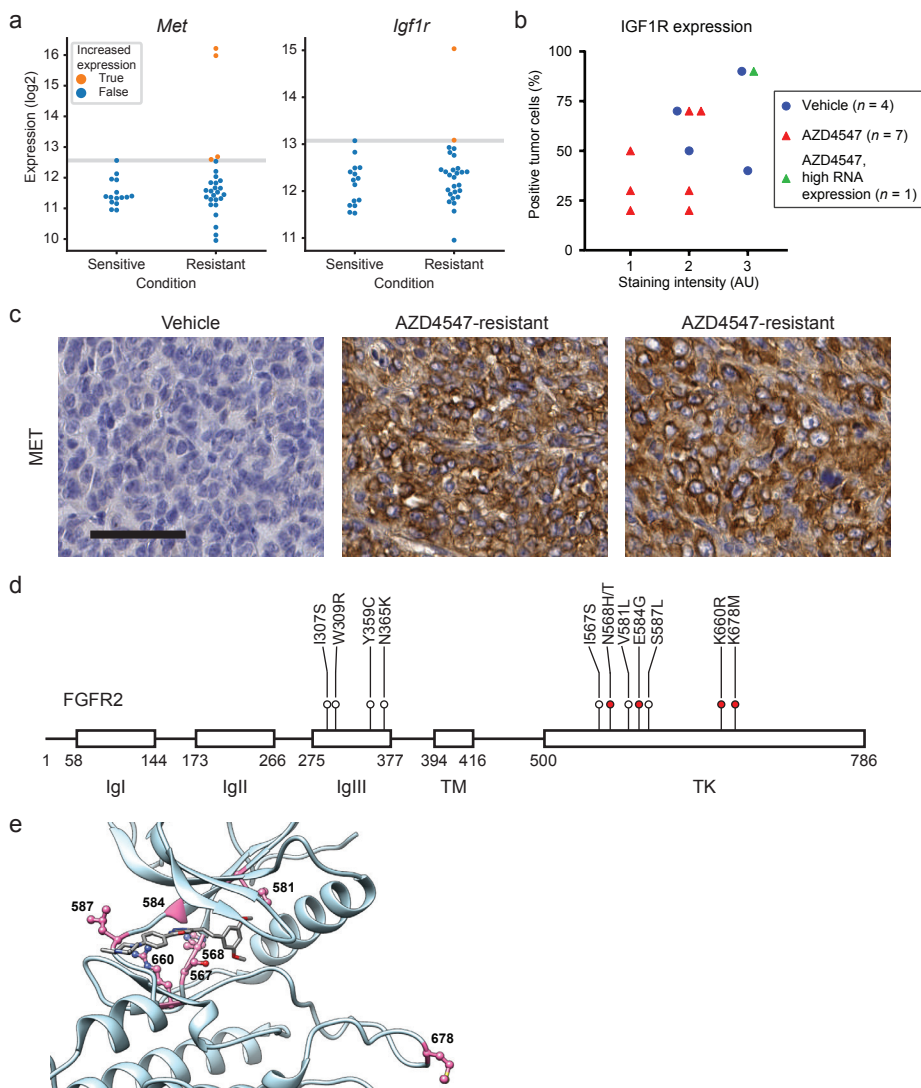


Figure 2: Transcriptome analysis of AZD4547-resistant tumors (a) Differential expression analysis of *Met* and *Igf1r* in AZD4547-sensitive ($n = 15$) and -resistant ($n = 27$) tumors using DIDS, showing outliers for *Met* ($n = 2$) and *Igf1r* ($n = 1$). (b) Quantification of IGF1R expression in AZD4547-sensitive ($n = 4$) and -resistant ($n = 8$) tumors. AU, arbitrary unit. (c) Representative immunohistochemical stainings of MET in AZD4547-sensitive (vehicle) and -resistant tumors. Scale bar, 50 μ m. (d) Schematic overview showing the locations of mutations identified for *Fgfr2* in the AZD4547-resistant tumors. Red mutations have been previously reported in patients with *FGFR2* fusion-positive cholangiocarcinoma, whose tumors acquired resistance to the selective FGFR inhibitor NVP-BGJ398. Numbers indicate amino acid residue positions (mouse). Ig, immunoglobulin-like domain; TM, transmembrane domain; TK, tyrosine kinase domain. (e) *In silico* modeling of AZD4547 (middle) in the ATP-binding pocket of FGFR2. The FGFR2 kinase domain is depicted as a sky-blue ribbon with residues of interest colored by atom type: carbon, pink; nitrogen, blue; oxygen, red. AZD4547 is colored by atom type: carbon, gray; nitrogen, blue; oxygen, red.

RNA-sequencing data to identify mutations in the above-mentioned RTKs and genes involved in the MAPK-ERK signaling pathway (Supplementary Table S2). Using this approach, we identified 12 missense mutations in *Fgfr2* affecting 11 different amino acids, of which 4 were located in the third immunoglobulin (Ig)-like domain (IgIII) and 7 were located in the tyrosine kinase domain (Fig. 2d).

To predict the effects of the mutations in the FGFR2 kinase domain on AZD4547 binding, we mapped the 7 missense mutations onto the FGFR2 protein structure and observed that residues I567, N568, V581, E584, S587 reside in the ATP-binding pocket of FGFR2 (Fig. 2e). As a consequence, these mutated residues directly perturb the binding site of AZD4547. In addition, the E584G mutation is located in the kinase hinge and introduces flexibility at the key recognition motif for AZD4547. The K660R mutation is adjacent to the binding site, which suggests that the binding of AZD4547 is indirectly perturbed. Finally, the K678M mutation is located in the kinase activation loop, suggesting that this mutation alters the dynamics of the activation loop and favors the active conformation.

Interestingly, 4 out of the 7 missense mutations in the tyrosine kinase domain reflected recurrent point mutations that were previously reported in patients with *FGFR2* fusion–positive cholangiocarcinoma, whose tumors acquired resistance to the selective FGFR inhibitor NVP-BGJ398¹⁰. In this previous work, structural characterization combined with functional *in vitro* studies showed that these FGFR2 kinase mutations either induce a steric clash with NVP-BGJ398 in the ATP-binding pocket or destabilize the inactive conformation of the kinase. Together, these data indicate that the 7 mutations in the ATP-binding pocket of FGFR2 disrupt the binding of selective FGFR tyrosine kinase inhibitors and therefore hamper their therapeutic efficacy.

AZD4547-resistant *SB*-induced tumors show *de novo* insertions in candidate resistance genes

Due to the presence of a constitutively active *SB* transposase, the *SB*-induced mILCs could be capable of developing resistance by acquiring *de novo* transposon insertions in or near resistance genes during AZD4547 treatment. To determine if *SB*-mediated mutagenesis might indeed be driving resistance in some of these tumors, we performed an insertion analysis of 27 AZD4547-resistant *SB*-induced tumors and compared the

identified *SB* insertions to those found in the donor tumor and 15 vehicle-treated tumors. Globally, this analysis showed that the majority of the clonal insertions in the donor tumor (e.g. *Fgfr2*, *Ppp1r12a*, *Slc16a9* and *Trps1*) were maintained after orthotopic transplantation and long-term treatment of the tumor-bearing mice (Supplementary Fig. 4a, Supplementary Table S1, S3). Interestingly, additional *SB* insertions were observed in both vehicle- and AZD4547-treated tumors, indicating that mobilization of transposons still occurs after transplantation of *SB*-induced tumors.

To specifically identify *de novo* insertions that might be driving resistance to AZD4547, we filtered for genes that contained *SB* insertions in the AZD4547-resistant tumors but not in the donor or vehicle-treated tumors (Supplementary Fig. 4b). This analysis revealed three candidate resistance genes (*Abcg2*, *Rasa1* and *Pcdh15*) with insertions in at least three AZD4547-resistant tumors (Fig. 3a). Of these three genes, *Abcg2* contained several independent insertions that were mainly in the sense orientation and located upstream of the transcription start site (Fig. 3b), indicating that these insertions result in increased *Abcg2* expression. In support of this, these insertions coincided with increased mRNA and protein expression of ABCG2 (Fig. 3c and Supplementary Fig. 5a-c). Variable ABCG2 expression highlights intra-tumor heterogeneity in mechanisms of AZD4547 resistance. In contrast to *Abcg2*, *Rasa1* and *Pcdh15* contained either a mix of sense/antisense insertions or purely antisense insertions, suggesting that these genes are inactivated (Fig. 3d-g). Further analysis revealed decreased expression of exons downstream of the insertion sites in *Rasa1*, supporting inactivation of *Rasa1* via truncation of the gene, whereas expression of *Pcdh15* was not markedly affected.

To investigate whether insertions from the donor tumor might contribute to intrinsic treatment resistance, we compared the relative support scores of insertions between untreated tumors (vehicle-treated tumors and the donor tumor) and AZD4547-resistant tumors to determine if insertions in specific genes were enriched after AZD4547 treatment. This analysis identified six genes (*Arid1a*, *Myh9*, *Fbxw7*, *Matr3*, *Slc16a9* and *Map4k4*) with increased support scores in AZD4547-resistant tumors, indicating that sub-clones with insertions in these genes are selected for during treatment (Supplementary Fig. 5d). These genes might therefore be involved in intrinsic resistance to AZD4547. Interestingly, the top three genes (*Arid1a*, *Myh9* and *Fbxw7*) were previously identified as candidate driver genes in ILC formation¹⁹.

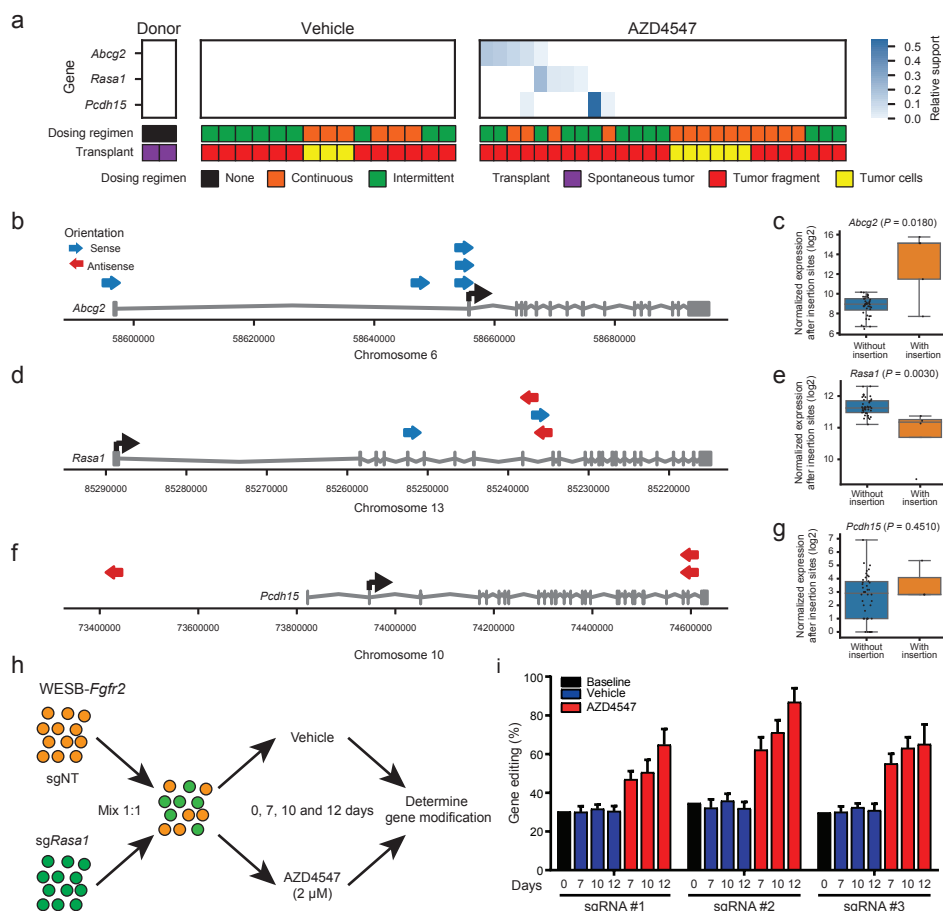


Figure 3: Overview of insertions and corresponding gene expression of candidate resistance genes (a) Overview of insertions in candidate resistance genes that were mutated in at least three AZD4547-resistant tumors ($n = 27$) and were not mutated in any of the donor (two technical replicates) or vehicle-treated ($n = 15$) tumors. Relative clonality of insertions is indicated by “relative support” scores (blue), which were calculated by counting the number of mate pairs supporting an insertion and normalizing these “support” scores to the highest score of the corresponding sample. (b–g) Left, visualization of *SB* insertions (arrows) in *Abcg2* (b), *Rasa1* (d), and *Pcdh15* (f). Right, normalized gene expression values after the insertion sites of *Abcg2* (c), *Rasa1* (e), and *Pcdh15* (g) in all *SB*-induced tumors with and without insertions in the respective genes. P values were calculated using a Mann–Whitney U test, as implemented in IM-Fusion. (h) Schematic overview of the *in vitro* competition assay performed with WESB-*Fgfr2* cells transfected with modified pX330 vectors containing sgRNAs targeting *Rasa1* (sg*Rasa1*) or a nontargeting sgRNA (sgNT). (i) Competition assay of WESB-*Fgfr2*-sgNT and WESB-*Fgfr2*-sg*Rasa1* cells mixed in a 1:1 ratio at day 0. After 7, 10, and 12 days of vehicle or AZD4547-treatment (2 μ mol/L), the allele distributions of the polyclonal populations were quantified by the percentage of frameshift mutations in *Rasa1* using the TIDE algorithm²⁹. The percentages of gene modifications are mean \pm SD of at least four replicates.

Collectively, these results show that persistent mobilization of transposons in *SB*-induced mILCs allows them to acquire new insertions during treatment and that this approach can be used to identify novel resistance mechanisms. Our analysis implicates upregulation of *Abcg2* and inactivation of *Rasa1* as additional resistance mechanisms to AZD4547, which were not previously identified with our mutational analyses. This demonstrates that combining insertional mutagenesis with drug treatments poses an effective strategy for identifying resistance mechanisms to targeted therapies in mice.

Loss of *RASA1* reduces sensitivity of WESB-*Fgfr2* tumor cells to AZD4547

To test whether inactivation of *Rasa1* induces resistance to AZD4547 treatment, we transfected WESB-*Fgfr2* tumor-derived cells with modified pX330 vectors containing single guide RNAs (sgRNAs) targeting three different genomic regions of *Rasa1* or a non-targeting sgRNA (sgNT). All the *Rasa1* targeting sgRNAs induced efficient modification of the *Rasa1* target sites in the transfected cell populations (Supplementary Fig. 5e-g), as determined by TIDE (tracking of insertions or deletions [indels] by decomposition) analysis²⁹. To test for drug sensitivity, we performed an *in vitro* competition assay with a mixture of WESB-*Fgfr2*-sgNT and WESB-*Fgfr2*-sg*Rasa1* cells (1:1 ratio) in the presence or absence of 2 μ M AZD4547 and subsequently quantified the allele distribution of the polyclonal population using the frequency of frameshift mutations in *Rasa1* (Fig. 3h). After prolonged AZD4547 treatment, the polyclonal population was enriched for *Rasa1* frameshift mutations for all three *Rasa1*-targeted regions (Fig. 3i), indicating that *Rasa1*-depleted cells were less sensitive to AZD4547 treatment compared to control cells. In contrast, the allele distributions were not affected when cells were cultured without AZD4547, demonstrating that the observed effect was not due to a difference in proliferation between WESB-*Fgfr2*-sgNT and WESB-*Fgfr2*-sg*Rasa1* cells. Altogether, these data show that inactivation of *Rasa1* reduces the sensitivity of WESB-*Fgfr2* cells to AZD4547 treatment.

AZD4547 is a substrate of ABCG2

Abcg2 is an ATP-binding cassette (ABC) efflux transporter, suggesting that overexpression of this gene may induce resistance through increased extrusion of AZD4547 from the tumor cells. To determine if this is indeed the case, we first sought to confirm that AZD4547 is a substrate for the ABCG2 transporter. To this end, we performed a vesicular transport assay

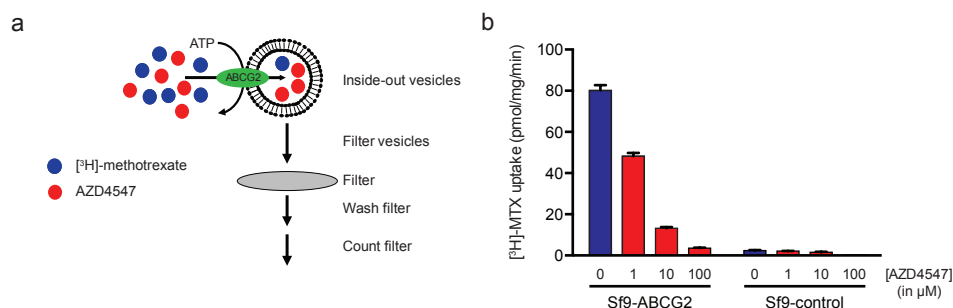


Figure 4: AZD4547 is a substrate for ABCG2 (a) Schematic overview of the vesicular transport assay. Control or ABCG2-containing inside-out membrane vesicles were incubated with $[^3\text{H}]$ -MTX (blue) and increasing concentrations of AZD4547 (red) in the presence or absence of ATP. After 10 minutes incubation, the membrane vesicles were captured using rapid filtration and the filters were washed to eliminate the excess of $[^3\text{H}]$ -MTX that was not transported into the vesicles. The retained radioactivity inside the membrane vesicles was measured using liquid scintillation counting. (b) Inhibition of ABCG2-mediated $[^3\text{H}]$ -MTX transport by increasing concentrations of AZD4547 (red). Values are corrected for transport in the absence of ATP. Data are mean \pm SD of three independent experiments, which were each performed in triplicate.

(Fig. 4a), in which we measured the uptake of tritium-labeled methotrexate ($[^3\text{H}]$ -MTX) in inside-out Sf9-membrane vesicles expressing ABCG2 (Sf9-ABCG2), both in the presence and absence of increasing concentrations of AZD4547, and compared the results to the uptake of $[^3\text{H}]$ -MTX in control Sf9-membrane vesicles (Sf9-control). This showed that ATP-dependent uptake of $[^3\text{H}]$ -MTX by ABCG2 was inhibited by AZD4547 (Fig. 4b), indicating that AZD4547 is indeed a substrate of ABCG2.

Overexpression of ABCG2 reduces sensitivity to AZD4547

To further explore whether increased expression of *Abcg2* reduces the sensitivity of cells to AZD4547, we used mouse embryonic fibroblasts (MEFs) derived from *Abcb1a*^{-/-};*Abcb1b*^{-/-};*Abcc1*^{-/-} mice (hereafter referred to as MEF3.8), which have very low background expression of endogenous ABCG2²¹. Furthermore, these MEFs lack both P-glycoprotein (P-gp, encoded by *Abcb1a* and *Abcb1b*), and the multidrug resistance-associated protein 1 (MRP1, encoded by *Abcc1*), allowing us to exclude confounding influences of these other drug efflux transporters. To test for drug sensitivity, MEF3.8 cells were transduced with an empty retroviral expression vector (MEF3.8-EV) or a vector containing *Abcg2* (MEF3.8-ABCG2) and subsequently exposed to increasing concentrations of AZD4547 in long-term clonogenic assays (Fig. 5a). Compared to MEF3.8 cells, MEF3.8-ABCG2 cells were

able to survive higher concentrations of AZD4547 (Fig. 5b, 5c), indicating that increased ABCG2 expression reduces the efficacy of AZD4547.

To confirm that increased expression of ABCG2 also reduces the sensitivity of treatment-naïve WESB-*Fgfr2* cells to AZD4547, we transduced these cells with an empty retroviral expression vector (WESB-*Fgfr2*-EV) or a vector containing *Abcg2* (WESB-*Fgfr2*-ABCG2) and treated the transduced cells with AZD4547. Short-term treatment of WESB-*Fgfr2*-EV cells with AZD4547 resulted in decreased phosphorylation of FGFR, FRS2 α and ERK1/2, whereas the phosphorylation levels of these proteins were less affected in AZD4547-treated WESB-*Fgfr2*-ABCG2 cells (Fig. 5d).

To test the effect of ABCG2 overexpression on the responsiveness of established tumors to AZD4547, we injected WESB-*Fgfr2*-EV and WESB-*Fgfr2*-ABCG2 cells into the mammary glands of immunocompromised NMRI-nude mice and these animals were treated with either vehicle or AZD4547 (12.5 mg/kg/day) daily for 30 days when the tumors reached the size of 62.5 mm³. Interestingly, the NMRI-nude mice did not show tumor regression upon treatment with AZD4547, in contrast to the previously used FVB syngeneic animals (Supplementary Fig. 2b), suggesting that an intact immune system might enhance the therapeutic efficacy of AZD4547. Nonetheless, mice with WESB-*Fgfr2*-EV tumors did show stable disease, whereas WESB-*Fgfr2*-ABCG2 tumors progressed during treatment (Fig. 5e-g). These results show that increased ABCG2 expression also reduces the sensitivity of FGFR2-activated tumors to AZD4547 *in vivo*, confirming that upregulation of this drug efflux transporter can drive resistance to AZD4547.

Discussion

In this work, we performed an *SB*-based insertional mutagenesis screen in a mouse model of ILC to identify genes that are involved in the development of resistance to FGFR-targeting therapies. As a starting point for this screen, we used *SB*-induced mILCs, in which we previously identified *Fgfr2* as the most frequently mutated candidate gene¹⁹. By orthotopically transplanting an *SB*-induced mILC with activated FGFR signaling into multiple recipient mice, we showed that treatment with the FGFR inhibitor AZD4547 initially results in tumor regression and provides long-term tumor control, but eventually results in acquired treatment resistance. Our mutational analysis of the AZD4547-resistant tumors identified several potential resistance

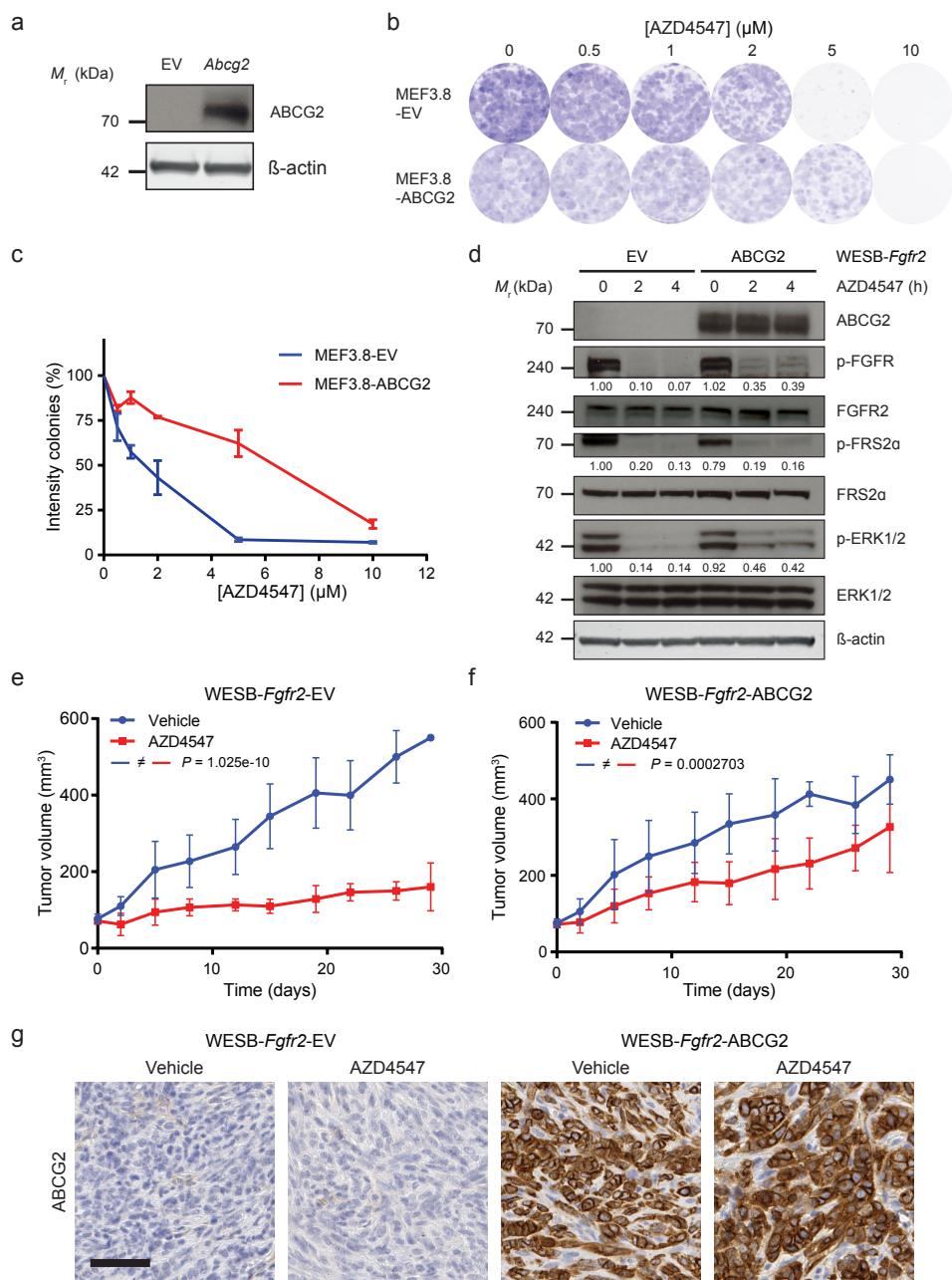


Figure 5: ABCG2 reduces sensitivity to AZD4547 *in vitro* and *in vivo* (a) Representative immunoblot ($n = 3$) for the expression of ABCG2 in MEF3.8-EV and MEF3.8-ABCG2 cells. β -Actin was used as a loading control. (b, c) Representative images (b) and quantification (c) of the clonogenic assays (11 days after seeding the cells) of MEF3.8 cells treated with increasing concentrations of AZD4547. Data are mean \pm SD of three independent experiments. (d) Representative immunoblot ($n = 3$) showing the effect of short-term AZD4547 treatment

mechanisms, including secondary mutations in FGFR2, inactivation of RASA1, a negative regulator of RAS signaling, and overexpression of MET and the drug-efflux transporter ABCG2. Together, these mechanisms explain acquired resistance to AZD4547 in (21 out of 27) tumors (Fig. 6a). Resistance mechanisms in the remaining 6 tumors remain to be identified.

In line with previous studies in a mouse model of melanoma³⁰ and *Arf*^{-/-} mice³¹, we show that transposon mutagenesis in mice can not only be used to identify candidate cancer genes, but is also an effective strategy to identify genes involved in *in vivo* drug resistance. In our mutational analysis of the AZD4547-resistant tumors, we exploited the constitutive activity of the *SB*-mediated insertional mutagenesis system in *SB*-induced mILCs to identify potential resistance mechanisms in an unbiased, genome-wide fashion. This allowed us to identify two resistance mechanisms (activation of ABCG2 and inactivation of RASA1), which might not have been identified without *SB* mutagenesis. On the other hand, resistance mechanisms that involve specific amino acid substitutions may not be uncovered by transposon mutagenesis, but only arise from spontaneous mutations. A comprehensive characterization of the various mechanisms of resistance to targeted anti-cancer therapeutics may therefore require a multipronged approach, combining transposon mutagenesis with other sequencing modalities to identify spontaneous mutations and/or transcriptional changes that may be driving resistance. Given enough sequencing depth, RNA-sequencing based approaches for identifying transposon insertions may be able to provide the most comprehensive analysis from a single dataset^{26,32}, by allowing detection of transposon insertions, mutations, gene-fusions and transcriptional changes in RNA-sequencing data. However, targeted DNA-sequencing approaches (as we have used here to detect *SB* transposon insertions) are likely to yield more detailed detection of insertions and/or mutations with a low frequency, by effectively providing deeper sequencing at a lower cost.

The diverse spectrum of identified resistance mechanisms illustrates the

←
(100 nmol/L) in WESB-*Fgfr2* cells with and without ABCG2 expression. β -actin was used as a loading control. **(e, f)** Tumor growth kinetics of WESB-*Fgfr2*-EV **(e)** and WESB-*Fgfr2*-ABCG2 **(f)** cells in NMRI-nude female mice under vehicle (blue) or AZD4547 (red) treatment (for 30 consecutive days). Datapoints are mean \pm SD and *P* values were calculated using mixed linear models (details are described in the Supplementary Data). Vehicle-treated WESB-*Fgfr2*-EV versus WESB-*Fgfr2*-ABCG2 tumors, *P* = 0.5511, not significant; AZD4547-treated WESB-*Fgfr2*-EV versus WESB-*Fgfr2*-ABCG2 tumors, *P* = 3.983e-05. **(g)** IHC detection of ABCG2 in sections of WESB-*Fgfr2*-EV and WESB-*Fgfr2*-ABCG2 tumors. Scale bar, 50 μ m.

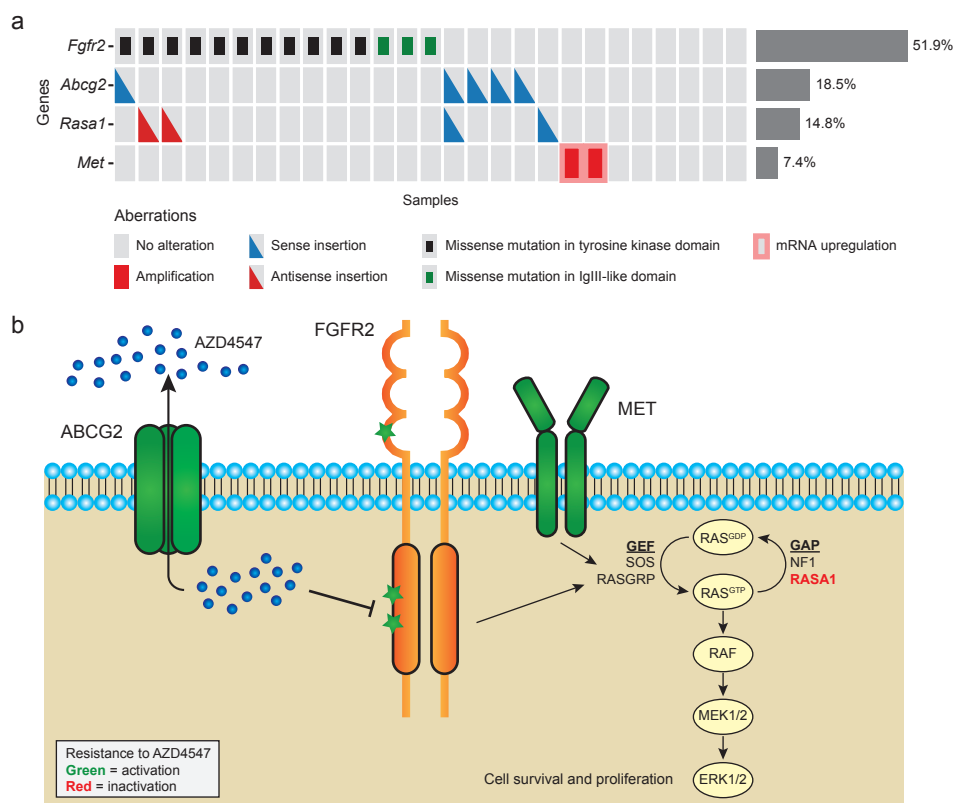


Figure 6: Schematic overview of the resistance mechanisms in AZD4547-resistant tumors identified in this study (a) Overview of the genetic alterations and gene expression changes in the respective genes identified in the AZD4547-resistant tumors. Red bars, amplification of the respective gene. Blue and red triangles indicate insertions in sense or antisense orientation relative to the gene, respectively. Bars with a red outline indicate the upregulation of the respective genes. Green and black squares represent missense mutations in the IgIII-like domain or the tyrosine kinase domain of FGFR2, respectively. **(b)** Schematic representation of the identified resistance mechanisms in the FGFR signaling pathway. Activating and inactivating events resulting in resistance to AZD4547 are depicted in green and red, respectively.

major challenge that (intra-) tumor heterogeneity poses for the prevention of therapy resistance, as we observe multiple resistance mechanisms arising from and within a single (donor) tumor. All of the identified mechanisms center on reactivation of the canonical MAPK-ERK signaling pathway, suggesting that this is a dominant mechanism for overcoming vulnerability to FGFR inhibition (Fig. 6b). Reactivation of MAPK-ERK signaling has also been identified as a predominant resistance mechanism to EGFR inhibitors³³. In our analysis of AZD4547-resistant tumors, we observed recurrent alterations in several components of the MAP-ERK

pathway, including secondary mutations in FGFR2, overexpression of the MET receptor and inactivation of RASA1. MET overexpression can induce resistance by driving reactivation of signaling pathways downstream of FGFR2, as has previously been shown in the context of FGFR and other RTK inhibitors^{2,14,15,34}. Also loss of RASA1, which is a negative regulator of RAS, may cause resistance to FGFR inhibition via reactivation of the MAPK-ERK pathway³⁵.

Our analysis of the secondary mutations in FGFR2 showed that the majority of these mutations occurred in the tyrosine kinase domain, suggesting that they mainly provide resistance by preventing the inhibitor from binding to the ATP-binding pocket and thereby reactivating the FGFR signaling pathway. This finding agrees with previous studies with other FGFR inhibitors, which identified polyclonal secondary FGFR mutations (including gatekeeper mutations) as a main resistance mechanism to FGFR-targeting treatments^{10–12}. Our observations are further supported by studies with other RTK inhibitors, which also describe secondary mutations in the receptor as one of the main resistance mechanisms to tyrosine kinase inhibitors³⁴.

Our validation of the drug efflux transporter *Abcg2* showed that increased ABCG2 expression can induce resistance by reducing the concentration of AZD4547 within tumor cells, which results in decreased inhibition of FGFR and reactivation of the FGFR signaling pathway. In patients, overexpression of the drug efflux pump MDR1 (encoded by *ABCB1*) has been observed in chemotherapy-resistant ovarian cancer³⁶. Our results suggest that drug efflux transporters such as ABCG2 can not only drive therapy resistance in hematological malignancies³⁷, but may also have similar effects on therapy efficacy in solid tumors.

Recent approaches have aimed to overcome resistance to FGFR-targeting therapies either by combining multiple existing RTK inhibitors^{14,15}, or by designing irreversibly binding inhibitors such as FIIN-2, FIIN-3 and PRN1371^{38,39}, which cannot be disrupted as easily by secondary mutations in the receptor. However, our results suggest that combining FGFR and MEK/ERK inhibitors might be a more effective strategy, as this prevents reactivation of MAPK-ERK signaling. Additionally, to avoid resistance resulting from drug efflux transporters, novel inhibitors should be specifically designed to be poor substrates for common transporters. Alternatively, CRISPR/Cas9 genetic screens could be used to identify synthetic lethal interactions with FGFR inhibitors in the context of FGFR inhibitor-resistant tumors to design rational and more effective combination therapies to

overcome drug resistance⁴⁰.

In summary, *SB* insertional mutagenesis in mice is an effective tool to identify mechanisms of drug resistance. A comprehensive analysis of AZD4547-resistant mILCs, in which *SB*-based mutagenesis is combined with targeted DNA- and RNA-sequencing, allowed us to explain the mechanism of resistance in 78% of the resistant tumors, of which all converged to the reactivation of the canonical MAPK-ERK signaling cascade. Altogether, our findings suggest that FGFR-targeting drugs might be improved by designing FGFR inhibitors that are poor substrates of drug efflux transporters and irreversibly bind to the ATP-binding pocket of the receptor to prevent secondary mutations in the tyrosine kinase domain. In addition, combining these novel FGFR inhibitors with MEK/ERK inhibitors might be an even more effective strategy for preventing resistance to FGFR-targeted therapies.

Acknowledgements

We are grateful to Els Wagenaar, Sander Canisius, Chris Doornebal, Eline van der Burg and Ute Boon for providing technical suggestions and/or assistance with the experiments. We thank Alfred Schinkel (The Netherlands Cancer Institute, Amsterdam) for the MEF3.8 and MEF3.8-ABCG2 cells. We thank Elaine Kilgour, Lindsay Bridgett and Paul Smith (Oncology IMED, IMED Biotech Unit, AstraZeneca) for providing the AZD4547. We thank the NKI animal facility, RHPC computing facility, the animal pathology facility, the mouse clinic transgenic and intervention unit, the core facility molecular pathology and biobanking (CFMPB), and the genomics core facility for their expert technical support. Financial support was provided by the Netherlands Organization for Scientific Research (NWO: Cancer Genomics Netherlands (CGCNL), Cancer Systems Biology Center (CSBC), Netherlands Genomics Initiative (NGI) grant Zenith 93512009 (J. Jonkers), infrastructural grant from the National Roadmap for Large-Scale Research Facilities), the EU Seventh Framework Program (Infrafrontier-I3 project 312325 (J. Jonkers)), and the European Research Council (ERC Synergy project CombatCancer (J. Jonkers)). This work was carried out on the Dutch national e-infrastructure with the support of SURF Cooperative (e-infra160136 (J. Jonkers)). This work is part of the OncoCode Institute which is partly financed by the Dutch Cancer Society (KWF) (J. Jonkers).

Disclosure of Potential Conflicts of Interest

C. Phillips and P.D. Smith have ownership interest (including patents) in AstraZeneca PLC. L.F.A. Wessels reports receiving a commercial research grant from Genmab. No potential conflicts of interest were disclosed by the other authors.

Authors' Contributions

Conception and design: S.M. Kas, J.R. de Ruiter, J. Jonkers

Development of methodology: S.M. Kas, J.R. de Ruiter, K. Schipper, L. Bombardelli, A. Berns, J. Jonkers

Acquisition of data (provided animals, acquired and managed patients, provided facilities, etc.): S.M. Kas,, K. Schipper, A.P. Drenth, R. de Korte-Grimmerink, S. Mahakena, K. van de Wetering,

Analysis and interpretation of data (e.g., statistical analysis, biostatistics, computational analysis): S.M. Kas, J.R. de Ruiter, K. Schipper, C. Phillips, P.D. Smith, S. Klarenbeek, K. van de Wetering, L.F.A. Wessels, J. Jonkers

Writing, review, and/or revision of the manuscript: S.M. Kas, J.R. de Ruiter, C. Phillips, P.D. Smith, K. van de Wetering, L.F.A. Wessels, J. Jonkers

Administrative, technical, or material support (i.e., reporting or organizing data, constructing databases): E. Schut, L. Bombardelli, E. Wientjens, A.P. Drenth, R. de Korte-Grimmerink, A. Berns,

Study supervision: J. Jonkers

Supplementary experimental details

Cell viability assay

WESB cells were seeded in triplicate with 500 cells per well in 96-well plates. After 24 hours, the medium was refreshed with either DMSO (as a control) or AZD4547 with the indicated concentrations. Three days later, cell viability was assayed in an Envision plate reader (Perkin Elmer) using resazurin (cell titer blue; Promega).

Clonogenic assay

MEFs were trypsinized and 2000 cells were seeded in 6-well plates. After 24 hours, the medium was refreshed with either DMSO (as a control) or AZD4547 with the indicated concentrations. Eleven days later, the cells were fixed with 4% formalin in PBS and stained with 0.1% crystal violet in demineralized water. Quantification was performed by dissolving the crystal violet with 10% acetic acid in demineralized water and determining the absorbance at 590 nm. The experiment was performed three times.

Competition assay

WESB-*Fgfr2* cells were transfected with pX330.pgkpur constructs containing three independent sgRNAs targeting *Rasa1* (*sgRasa1*) or a non-targeting as control (sgNT) using Lipofectamine 2000 (ThermoFisher Scientific 11668027) according to manufacturer's protocol. Transfected cells were selected using puromycin (4 µg/ml) for 48 hours. The pX330.pgkpur construct is a modified version of the pX330 backbone ⁴¹, which contains a puromycin resistance ORF under the hPGK promoter ⁴². The pX330-U6-Chimeric_BB-CBh-hSpCas9 construct was a gift from Dr Feng Zhang (Addgene plasmid #42230). WESB-*Fgfr2* cells containing sgNT or *sgRasa1* were mixed and seeded at a one-to-one ratio on 6-well plates in medium supplemented with 5% FBS and either DMSO or 2 µM AZD4547. The medium was refreshed every 4 days and DNA was isolated at days 0, 7, 10 and 12 using the Gentra Puregene genomic DNA isolation kit (Qiagen). PCR amplifications of *Rasa1* exon 2, 6 and 8 were performed with specific primers spanning the target sites and 100-200 ng DNA template, using the Q5 High-Fidelity PCR kit (NEB M0492). Amplification PCR reactions were diluted 20 times with Milli-Q and subsequently Sanger sequenced using the FW primers. CRISPR/Cas9-induced editing efficacy was quantified using the TIDE algorithm ²⁹. Cells with only sgNT were used as a negative control in all genomic DNA amplifications and only TIDE outputs with $R^2 > 0.9$ were considered.

sgRNA sequence *Rasa1*-1: 5'-TTATAAGAGAGAGTGATCGG-3'

sgRNA sequence *Rasa1*-2: 5'-CGAGAAGAAGATCCACACGA -3'

sgRNA sequence *Rasa1*-3: 5'-ATCTCCAGGAGTATTATCTG-3'

Rasa1 sgRNA1 PCR FW 5'-TTGTGTTCTCACAGACCTGAAT-3' (557 bp)
Rasa1 sgRNA1 PCR RV 5'-TCAATCTGTGATCTCCAAGCC-3' (557 bp)
Rasa1 sgRNA2 PCR FW 5'-TGTAGGCAAGAGAGCCAAATTA-3' (697 bp)
Rasa1 sgRNA2 PCR RV 5'-GTTCAAGGCCAGTCTGATCTAC-3' (697 bp)
Rasa1 sgRNA3 PCR FW 5'-GAGTTCTTTCAGAGAGCGAAGG-3' (406 bp)
Rasa1 sgRNA3 PCR RV 5'-GAGTTCTTTCAGAGAGCGAAGG-3' (406 bp)

Preparation of membrane vesicles and vesicular transport assays

Membrane vesicles from Sf9 cells were obtained after infection with a control or a human ABCG2-containing baculovirus at a multiplicity of infection of 1²². After incubation at 27°C for 3 days, cells were harvested by centrifugation at 500 x *g* for 5 min. Cells were then resuspended in ice-cold hypotonic buffer (0.5 mM sodium phosphate and 0.1 mM EDTA, pH 7.4) supplemented with a protease inhibitor cocktail (Roche, Basel, Switzerland) and incubated at 4°C for 90 min under constant agitation. Thereafter, the cell lysate was homogenized using a tight-fitting Dounce homogenizer. Next, cell debris and nuclei were removed by slow-speed centrifugation at 500 x *g* (4°C for 10 min). The supernatant was collected and centrifuged at 4°C at 100,000 x *g* for 40 min. The membrane pellet was resuspended in TS buffer (50 mM Tris-HCl and 250 mM sucrose, pH 7.4) and passed through a 27-gauge needle 25 times. The vesicles were dispensed in aliquots, snap-frozen in liquid nitrogen, and stored at -80°C until use. Vesicular transport assays were performed using the rapid filtration method as previously described^{22,23}. Briefly, ABCG2 or control Sf9 membrane vesicles containing 20 µg of protein were incubated with 1 µM [³H]-MTX in 50 µl of TS buffer in the presence of 4 mM ATP or AMP, 10 mM MgCl₂, 10 mM creatine phosphate, and 100 g of creatine kinase/ml. After 10 minutes, 40 µl of the reaction mixture was diluted in 200 µl of ice-cold TS buffer and immediately filtrated using a MultiScreen_{HTS} vacuum manifold in combination with Multiscreen_{HTS} FB 96-well filter plates (Millipore, Bedford, MA). Membranes were washed four times with 200 µl of ice-cold phosphate-buffered saline and the radioactivity retained on the membranes was counted by liquid scintillation counting.

Immunohistochemistry

Tissues were formalin-fixed and paraffin-embedded (FFPE) by routine procedures. Immunohistochemical stainings of MET, ABCG2 (BCRP) and cleaved Caspase-3 were processed as previously described^{20,43}. The following primary antibodies were used for the respective proteins: MET (1:100, R&D Systems AF527), BCRP (1:400, Abcam 24115) and cleaved Caspase-3 (1:400, CST 9661). Citrate buffer was used as antigen retrieval for MET and BCRP. TRIS/EDTA pH 9.0 was used for cleaved Caspase-3. Immunohistochemical staining of IGF1R was performed on a Discovery Ultra autostainer (Ventana Medical Systems). Briefly, paraffin sections were cut at 3 μ m, heated at 75°C for 28 minutes and deparaffinised in the instrument with EZ prep solution (Ventana Medical Systems). Heat-induced antigen retrieval was carried out using Cell Conditioning 1 (CC1, Ventana Medical Systems) for 64 minutes at 95°C. IGF1R was detected using clone G11 (Ready-to-use, 16 minutes at 37°C, Ventana Medical Systems), bound antibody was detected using the OMap anti-Rb HRP (Ventana Medical Systems) for 12 minutes after which the ChromoMap DAB Kit (Ventana Medical Systems) was applied. Slides were counterstained with Hematoxylin and Bluing Reagent (Ventana Medical Systems). All slides were digitally processed using the Aperio ScanScope (Aperio, Vista, CA, USA) and captured using ImageScope software version 12.3.2.8013 (Aperio). Cleaved Caspase-3 and ABCG2 immunohistochemical stainings were reviewed and scored by a veterinary pathologist (Sjoerd Klarenbeek) in a blinded manner. The images on the slides were captured using an Axioskop 40 microscope and an AxioCam MRc5 camera (Zeiss) and analyzed using the ZEN lite 2012 (Blue edition) software. The number of cleaved Caspase-3 positive cells were counted in four independent fields (0.34 mm²) per tumor and the average number of positive cells per mm² was calculated. Necrotic areas in these tumors were excluded from the analysis.

Immunoblotting

Protein lysates were made using lysis buffer (25 mM Tris-HCl pH 7.6, 150 mM NaCl, 1% NP-40, 1% sodium deoxycholate, 0.1% SDS in Milli-Q) complemented with protease and phosphatase inhibitors (Roche) and quantified using the BCA protein assay kit (Pierce). Equal amounts of proteins were separated on a 4-12% Bis-Tris gradient gel (Invitrogen) and transferred overnight onto nitrocellulose membrane (Bio-Rad) in 1x transfer buffer (25 mM Tris, 2 M Glycine, 20% methanol in demineralized

water). Membranes were blocked in 5% w/v bovine serum albumin (BSA) in PBS-T (pH 7.5, 0.005% Tween-20 in demineralized water) and incubated overnight with the primary antibodies in 5% w/v BSA in PBS-T. Membranes were washed three times and incubated with the secondary antibodies goat anti-rabbit-HRP (1:2000, Dako P0448), rabbit anti-mouse-HRP (1:5000, Dako P0260), rabbit anti-rat-HRP (1:2000, Invitrogen 61-9520) or donkey anti-mouse IRDye 680nm (1:5000, Li_COR 926-32222) in 5% w/v BSA in PBS-T. Stained membranes were washed three times in PBS-T and then developed using ECL (Pierce 32209), ECL 2 Substrate (Pierce 80196) or captured using the Li-Cor Odyssey Infrared Imaging System and analyzed using Odyssey Application software version 3.0.16. The intensities of the bands were quantified using ImageJ software version 2.0.0-rc-65/1.52b.

RNA sequencing and analysis

Illumina TruSeq mRNA libraries were generated and sequenced with 50-65 base single reads on a HiSeq 2500 using V4 chemistry (Illumina Inc., San Diego) as previously described by Boelens *et al.*⁴⁴. The resulting reads were trimmed using Cutadapt (version 1.13) to remove any remaining adapter sequences⁴⁵, filtering reads shorter than 20 bp after trimming to ensure good mappability. The trimmed reads were aligned to the GRCm38 reference genome using STAR (version 2.5.3a)⁴⁶. QC statistics from Fastqc (version 0.11.5; <http://www.bioinformatics.babraham.ac.uk/projects/fastqc>) and the above-mentioned tools were collected and summarized using Multiqc (version 1.1)⁴⁷. Gene expression counts were generated by featureCounts (version 1.5.2) using gene definitions from Ensembl GRCm38 version 89⁴⁸. Normalized expression values were obtained by correcting for differences in sequencing depth between samples using DESeqs median-of-ratios approach and then log-transforming the normalized counts⁴⁹. Differentially expressed genes were identified using DIDS (version 0.10.1)²⁸, using a threshold of $p < 0.05$ for statistical significance. Variants in RTKs and genes involved in downstream FGFR signaling were called using Vardict (version 2017.04.18) and annotated using Ensembl VEP (version 90.7)^{50,51}. The entire analysis pipeline (including the alignment, expression estimation and variant calling) was implemented using Snakemake and is freely available on GitHub [<https://github.com/jrderuiter/snakemake-rnaseq>]⁵².

Amplification of SB transposon insertions

Transposon insertions were amplified following a previously described

tagmentation-based DNA sequencing protocol²⁴. Briefly, recombinant Tn5 transposase was prepared as previously described by Picelli *et al.*⁵³, and diluted in glycerol buffer to a final concentration of 3.7 μ M. The Tn5-adapter complex was prepared by incubating 30 minutes at 37°C equimolar amounts of Tn5 and separately annealed adapters pairs Tn5ME-A+ 3'dT5P-oligo and Tn5ME-B+3'dT5P-oligo as previously described by David L. Stern²⁴. Each tagmentation reaction was prepared by combining 2 μ l of genomic DNA (100 ng in total), 4 μ l of 5x TAPS-PEG buffer⁵³, 1 μ l of Tn5-adapters complex and 13 μ l water and incubated for 10 minutes at 55°C. Tn5 was stripped off from DNA by adding 4 μ l of 0.2% SDS and incubating the reaction 5 min at 55°C. The enrichment PCR was performed by combining 3 μ l of tagmented DNA, 1 μ l of enrichment primer at 1 μ M, 6 μ l water and 10 μ l Phusion Flash 2x mix (cat.# F548L, Thermo Scientific, Waltham, MA USA). PCR1 was performed by combining 5 μ l of enrichment PCR reaction, 8 μ l water, 1 μ l of P5-indexed primer and 1 μ l of transposon-specific primer SB-PCR1 and 10 μ l Phusion Flash 2x mix. PCR2 was performed by combining 2 μ l of PCR1 reaction, 8 μ l water, 1 μ l of P7-indexed primer + 1 μ l FC2 primer and 10 μ l Phusion Flash 2x mix. Equal amounts of PCR2 products were pooled and run on an agarose gel. Fragments above 600 basepairs were excised from the gel, purified on Qiagen columns and eluted in water. The pool of tagmented DNA was sequenced with 150 base paired-end reads on a MiSeq 300 using the micro kit v2 reagents (Illumina Inc., San Diego). The following primer sequences and PCR cycler settings were used:

Primer sequences

SB-enrich: GCTTGTGGAAGGCTACTCGAAATGTTTGACCC

SB-pcr1: GTCTCGTGGGCTCGGAGATGTGTATAAGAGACAGGTGTATGTA-AACTTCCGACTTCAAC

FC2: AATGATACGGCGACCACCGA

Tn5ME-A-adaptor: TCGTCGGCAGCGTCAGATGTGTATAAGAGACAG

3'dT5P-oligo: CTGTCTCTTATACACATCTGAC (must be 5' phosphorylated and 3'OH blocked by an inverted thymidine)

Tn5ME-B-adaptor: GTCTCGTGGGCTCGGAGATGTGTATAAGAGACAG

A-idx-i5-1: AATGATACGGCGACCACCGAGATCTACACTAATGTGGTCGTCGGCAGCGTC

A-idx-i5-2: AATGATACGGCGACCACCGAGATCTACACGCACTCAGTCGTCGGCAGCGTC

A-idx-i5-3: AATGATACGGCGACCACCGAGATCTACACAACAGCGGTCGTCGGCAGCGTC
A-idx-i5-4: AATGATACGGCGACCACCGAGATCTACACCCATATGATCGTCGGCAGCGTC
A-idx-i5-5: AATGATACGGCGACCACCGAGATCTACACTGGAAGCTCGTCGGCAGCGTC
A-idx-i5-6: AATGATACGGCGACCACCGAGATCTACACAGCAACGCTCGTCGGCAGCGTC
A-idx-i5-7: AATGATACGGCGACCACCGAGATCTACACCCCTTGCATCGTCGGCAGCGTC
A-idx-i5-8: AATGATACGGCGACCACCGAGATCTACACCCCTTGTCTCGTCGGCAGCGTC
A-idx-i5-9: AATGATACGGCGACCACCGAGATCTACACTTCGAGCCTCGTCGGCAGCGTC
A-idx-i5-10: AATGATACGGCGACCACCGAGATCTACACAGTAGTTATCGTCGGCAGCGTC
A-idx-i5-11: AATGATACGGCGACCACCGAGATCTACACAGAAAGTGCTCGTCGGCAGCGTC
A-idx-i5-12: AATGATACGGCGACCACCGAGATCTACACTGCCGGTATCGTCGGCAGCGTC
A-idx-i5-13: AATGATACGGCGACCACCGAGATCTACACGAAACTGCTCGTCGGCAGCGTC
A-idx-i5-14: AATGATACGGCGACCACCGAGATCTACACGGTTGAGATCGTCGGCAGCGTC
A-idx-i5-15: AATGATACGGCGACCACCGAGATCTACACATAGATGTTCTCGTCGGCAGCGTC
A-idx-i5-16: AATGATACGGCGACCACCGAGATCTACACCAAACATTTCTCGTCGGCAGCGTC
A-idx-i5-17: AATGATACGGCGACCACCGAGATCTACACCTGAGCGTTCGTCGGCAGCGTC
B-idx-i7-1: CAAGCAGAAGACGGCATAACGAGATTCGCCTTAGTCTCGTGGGCTCGG
B-idx-i7-2: CAAGCAGAAGACGGCATAACGAGATATCCGCATGTCTCGTGGGCTCGG
B-idx-i7-3: CAAGCAGAAGACGGCATAACGAGATATTGAAGTGCTCTCGTGGGCTCGG
B-idx-i7-4: CAAGCAGAAGACGGCATAACGAGATCTCTGCGTGTCTCGTGGGCTCGG
B-idx-i7-5: CAAGCAGAAGACGGCATAACGAGATGATACGCAGTCTCGTGGGCTCGG
B-idx-i7-6: CAAGCAGAAGACGGCATAACGAGATTACGTTCTCGTGGGCTCGG
B-idx-i7-7: CAAGCAGAAGACGGCATAACGAGATTGAATCCTGTCTCGTGGGCTCGG
B-idx-i7-8: CAAGCAGAAGACGGCATAACGAGATGGCTATAAGTCTCGTGGGCTCGG
B-idx-i7-9: CAAGCAGAAGACGGCATAACGAGATCACAACCTGTCTCGTGGGCTCGG

PCR cycler settings

Enrichment PCR (2-step): 98°C 30s; 45 cycles of (98°C 8s, 72°C 35s)

PCR1: 98°C 30s; 15-18 cycles of (98°C 8s, 63°C 5s, 72°C 30s)

PCR2: 98°C 30s; 15-18 cycles of (98°C 8s, 63°C 5s, 72°C 30s)

Insertion site analysis

Insertion sites were identified using the taqmap pipeline in PylM (version 0.3.0, <https://github.com/jrderuiter/pyim>). Briefly, this analysis pipeline first trimmed the TaqMap paired-end reads using Cutadapt (version 1.12) to remove any matepairs not containing the transposon and to remove any Nextera transposase sequences⁴⁵. The remaining mate pairs were aligned to the mm10 reference genome using Bowtie2 (version 2.3.0)⁵⁴. After the alignment, redundant sequences mapping to the same genomic location and belonging to the same tumor were collapsed into a single insertion. To avoid issues with slight variations in the alignment, insertions from the same sample that occurred within 10 bp of each other were collapsed into a single insertion. Insertions were assigned to genes using the rule-based mapping approach⁵⁵ with the *SB* preset and gene definitions from Ensembl GRCm38 89. Support scores were calculated as the number of unique mate pairs supporting a given insertion. Relative support scores (used as a proxy for clonality) were calculated by normalizing support scores to the highest support score of the corresponding sample.

Genes associated with *de novo* resistance were identified by selecting genes that did not have any insertions in untreated tumors (vehicle-treated tumors and the donor tumor) and had insertions in at least two AZD4547-resistant samples. The *de novo* candidate genes were then ranked by their frequency of occurrence. Genes associated with intrinsic resistance were selected by performing a Welch's *t*-test between the clonality scores of insertions in the AZD4547-resistant tumors and the vehicle treated tumors, as well as determining the difference between the means of both groups (to ensure a minimum effect size). Candidate genes were selected by filtering for genes with a difference in means > 0.1 and a *t*-test *P* value < 0.25, after which the candidates were ranked by their mean differences.

Validation of the endogenous *Fgfr2-Tbc1d1* fusion

The *Fgfr2-Tbc1d1* fusion was detected in WESB-*Fgfr2* cells as previously described⁵⁶. WESB cells were used as negative control. The following primer sequences were used:

Fgfr2 FW: 5'-TGGCCAGGGATATCAACAAC-3'

Tbc1d1 RV: 5'-CCAGGCTGTGAGAAGGATTT-3'

Met qPCR copy number analysis

DNA was isolated from AZD4547-resistant tumors and wild-type FVB spleen as a control. The qPCR was performed on a Quantstudio 6 flex Real-Time PCR system (Applied Biosystems) using low ROX SYBR green (Bioline) with *Met* and β -catenin (*Ctnnb1*) specific primers.

Met FW: 5'-TCTCGGAGCCACAACTACA-3'

Met RV: 5'-GCAGTCCCGACAAGGTAAAC-3'

Ctnnb1 FW: 5'-TCAGGGCAGGTGAACTGTA-3'

Ctnnb1 RV: 5'-GACTCCCAGCACACTGAACTTA-3'

The relative copy number levels of *Met* and *Ctnnb1* were quantified using a five-point standard curve. The *Met* relative copy number was normalized to the *Ctnnb1* relative copy number for each sample and subsequently normalized to the normalized relative abundance of wild-type FVB spleen.

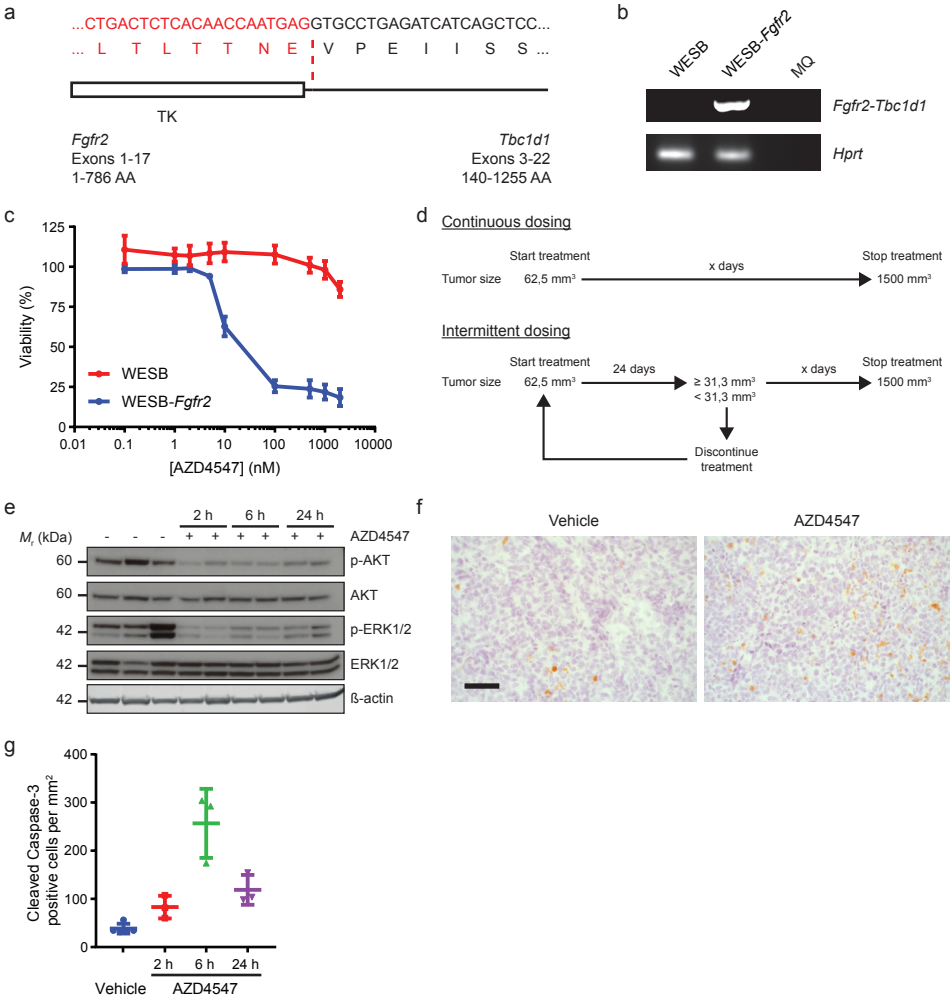
Statistical analysis

The effect of AZD4547 treatment on tumor growth of WESB-*Fgfr2*-EV and WESB-*Fgfr2*-ABCG2 established tumors was tested using mixed linear models. Prior to this analysis, the tumor size measurements were scaled so that each tumor's size at the first time point was equal to 1. Inspection of the individual tumor growth curves suggested an approximately linear increase in tumor size over time. The exact growth rate, i.e. the slope of the growth curve, showed some inter-tumor variability. Therefore, we modeled growth rate using a fixed effect population-level slope β , a random effect tumor-level slope b_i to account for inter-tumor variability, and a fixed effect term γ for the interaction of time and treatment to model the effect of treatment on tumor growth. Additional inter-tumor variability is allowed by random intercepts a_i , which complement the fixed effect intercept α . This leads to the following model formulation for the size of tumor i as a function of time and treatment:

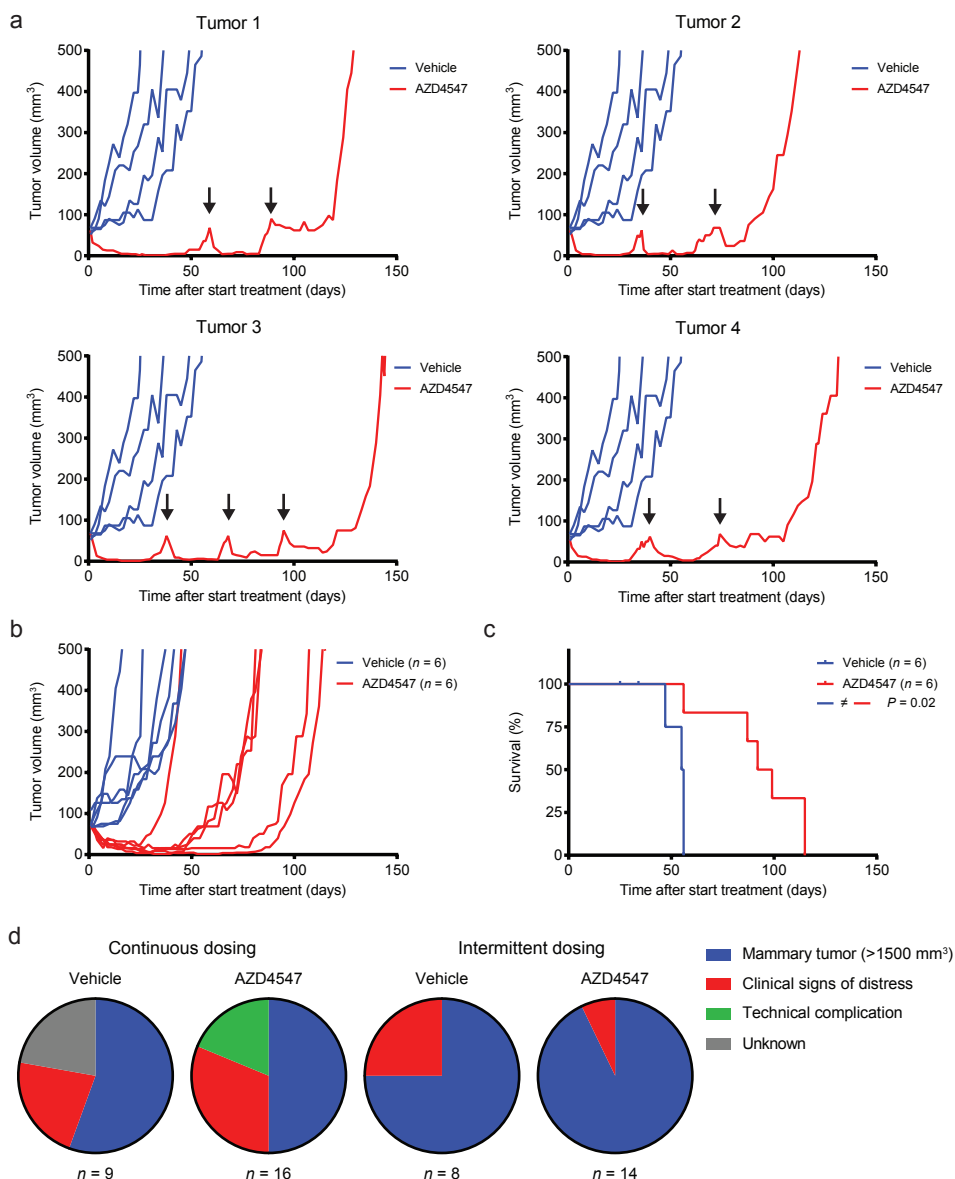
$$\text{Tumor size}_i = \alpha + a_i + (\beta + b_i) \times \text{time} + \gamma \times \text{time} \times \text{treatment}_i$$

The significance of the treatment effect was established using an ANOVA comparing the models with and without the interaction term γ .

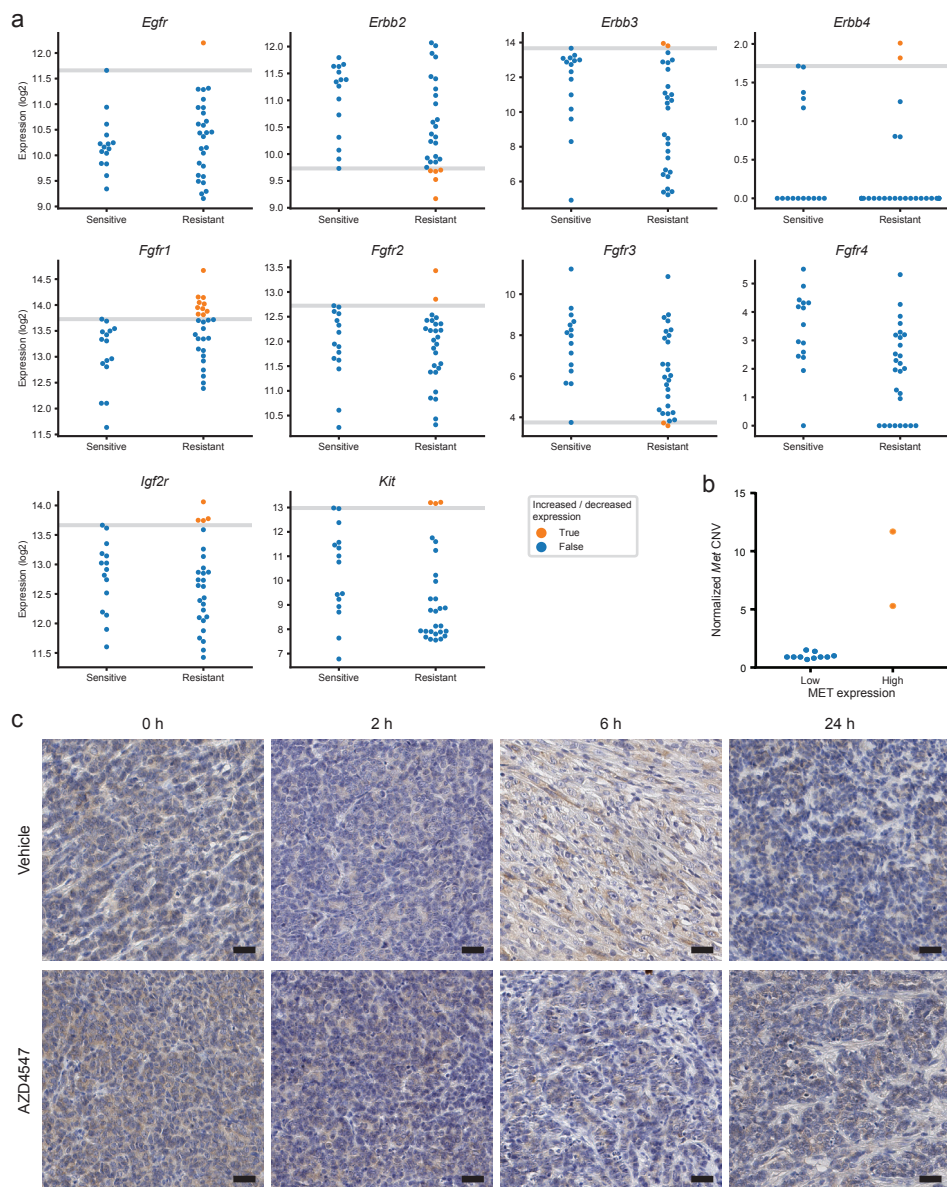
Supplementary Figures



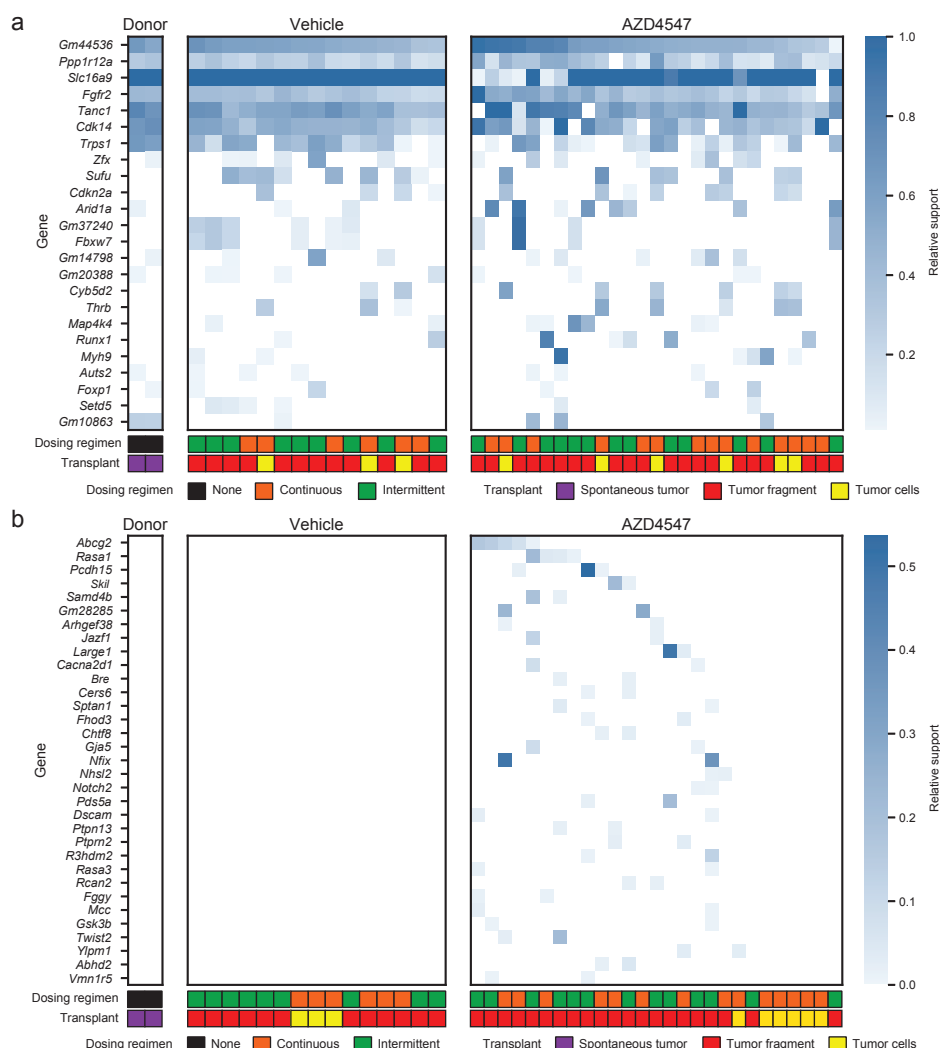
Supplementary Figure 1: Validation of the *Fgfr2-Tbc1d1* gene fusion and the effects of AZD4547 treatment on viability and downstream FGFR signaling in WESB cells. (a) Schematic overview of the *Fgfr2-Tbc1d1* gene fusion showing the genomic and amino acid sequences of *Fgfr2* (red) and *Tbc1d1* (black). (b) Validation of the *Fgfr2-Tbc1d1* fusion using targeted PCR on cDNA of WESB-Fgfr2 tumor-derived cells. WESB cells and MQ (= Milli-Q) were used as negative controls. (c) The viability of WESB and WESB-Fgfr2 cells after 72 hours of AZD4547 treatment. Data are mean \pm s.d. of three independent experiments in which the cells were seeded in triplicate. (d) Schematic representation of the treatment schedules with AZD4547 in tumor-bearing mice. (e) Immunoblot showing the effect of a single vehicle/AZD4547 treatment on total and phosphorylated AKT and ERK1/2 in established WESB-Fgfr2 tumors. β -actin was used as a loading control. (f,g) Representative images (f) and quantification (g) of immunohistochemical detection of cleaved Caspase-3 in tumors after a single vehicle ($n = 5$) or AZD4547 treatment ($n = 3$ for each indicated timepoint after administration of AZD4547). Scale bar, 50 μ m.



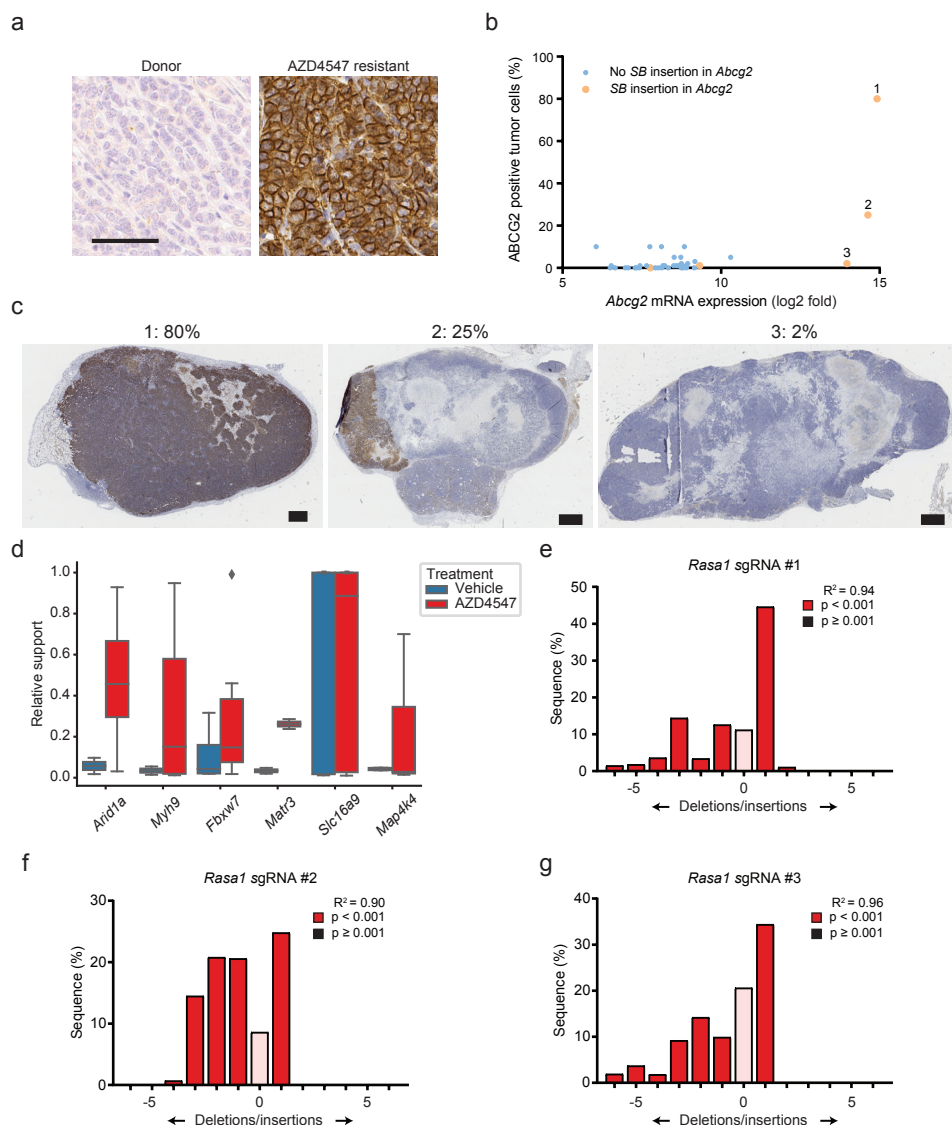
Supplementary Figure 2: Tumor growth kinetics of established tumors during treatment and causes of death observed under the different treatment schedules. (a) Tumor growth kinetics of vehicle (blue) and four different AZD4547-treated (red) tumors. The black arrows indicate the start of a treatment cycle of 24 days. (b) Tumor growth kinetics of WESB-*Fgfr2* cells injected into the mammary gland of wild-type syngeneic recipient female mice under continuous treatment with vehicle (blue) or AZD4547 (red). (c) Kaplan-Meier curve showing the overall survival of tumor-bearing mice upon continuous dosing with vehicle (blue) or AZD4547 (red). *P*-value was calculated using a Mantel-Cox test. (d) Comparison of the causes of death observed in the different treatment schedules.



Supplementary Figure 3: Differential gene expression analysis of multiple RTK family members and the status of MET in vehicle-treated, AZD4547-sensitive and resistant tumors. (a) Differential gene expression analysis of all FGFR-, EGFR-, IGF-related family members and *Kit* in AZD4547-sensitive ($n = 15$) and resistant ($n = 27$) tumors using DIDS. (b) Quantitative PCR (qPCR) of *Met* copy number variation (CNV) in AZD4547-resistant tumors with high ($n = 2$) or low ($n = 10$) MET expression. *Met* CNV is normalized to *Ctnnb1* (control). (c) Representative images of MET immunohistochemical stainings of WESB-Fgfr2 tumors after a single vehicle- or AZD4547-treatment. Scale bar, 25 μ m.



Supplementary Figure 4: Overview of insertions in genes across donor, vehicle-treated and AZD4547-resistant tumors. (a) Overview of insertions in genes across donor (two technical replicates), vehicle-treated ($n = 15$) and AZD4547-resistant ($n = 27$) tumors. Relative support scores of insertions (depicted in blue) were calculated by counting the number of mate pairs supporting the insertion and normalizing these 'support' scores to the highest score of the corresponding sample. (b) Overview of insertions in genes that were mutated in two or more AZD4547-resistant ($n = 27$) tumors but were not mutated in any of the donor or vehicle tumors. The relative support of the insertions within each sample is depicted in blue.



Supplementary Figure 5: Immunohistochemical stainings of ABCG2 in correlation to mRNA expression in AZD4547-resistant tumors, boxplots of genes that show intrinsic resistance to AZD4547 and efficacy of *Rasa1* gene editing in WESB-Fgfr2 cells. (a) Representative immunohistochemical stainings of ABCG2 in the WESB-Fgfr2 donor tumor and an AZD4547-resistant tumor. Scale bar, 50 μ m. (b) Correlation plot of mRNA and protein expression of ABCG2 in AZD4547-resistant tumors ($n = 27$) with and without insertions in *Abcg2*. (c) Immunohistochemical stainings of ABCG2 in the three AZD4547-resistant tumors with the highest *Abcg2* mRNA expression as depicted in (b). Scale bar, 1 mm. (d) Boxplot showing the relative support scores for genes that show enriched support in AZD4547-resistant compared to vehicle-treated tumors (differential support score > 0.1 and $P < 0.25$, t -test). (e-g) Representative spectrum of insertions and deletions (indels) for each sgRNA targeting *Rasa1* in WESB-Fgfr2 cells as quantified using the TIDE algorithm.

Supplementary tables (available online)

Supplementary Table 1

Overview of the sequenced tumor samples, including sample IDs, treatment information and the type of transplanted material.

Supplementary Table 2

Mutations (SNVs) identified for RTKs and genes involved in the MAPK-ERK signaling pathway in the donor, vehicle- and AZD4547-treated tumors.

Supplementary Table 3

Overview of insertions identified in the donor, vehicle- and AZD4547-treated tumors.

References

1. Ornitz, D. M. & Itoh, N. The Fibroblast Growth Factor signaling pathway. *Wiley Interdiscip. Rev. Dev. Biol.* 4, 215–266 (2015).
2. Babina, I. S. & Turner, N. C. Advances and challenges in targeting FGFR signalling in cancer. *Nat. Rev. Cancer* 17, 318–332 (2017).
3. Porta, R. *et al.* FGFR a promising druggable target in cancer: Molecular biology and new drugs. *Crit. Rev. Oncol. Hematol.* 113, 256–267 (2017).
4. Chae, Y. K. *et al.* Inhibition of the fibroblast growth factor receptor (FGFR) pathway: the current landscape and barriers to clinical application. *Oncotarget* 8, 16052–16074 (2017).
5. André, F. *et al.* Targeting FGFR with dovitinib (TKI258): preclinical and clinical data in breast cancer. *Clin. Cancer Res. Off. J. Am. Assoc. Cancer Res.* 19, 3693–3702 (2013).
6. Nogova, L. *et al.* Evaluation of BGJ398, a Fibroblast Growth Factor Receptor 1-3 Kinase Inhibitor, in Patients With Advanced Solid Tumors Harboring Genetic Alterations in Fibroblast Growth Factor Receptors: Results of a Global Phase I, Dose-Escalation and Dose-Expansion Study. *J. Clin. Oncol. Off. J. Am. Soc. Clin. Oncol.* 35, 157–165 (2017).
7. Tabernero, J. *et al.* Phase I Dose-Escalation Study of JNJ-42756493, an Oral Pan-Fibroblast Growth Factor Receptor Inhibitor, in Patients With Advanced Solid Tumors. *J. Clin. Oncol. Off. J. Am. Soc. Clin. Oncol.* 33, 3401–3408 (2015).
8. Javle, M. *et al.* Phase II Study of BGJ398 in Patients With FGFR-Altered Advanced Cholangiocarcinoma. *J. Clin. Oncol. Off. J. Am. Soc. Clin. Oncol.* JCO2017755009 (2017) doi:10.1200/JCO.2017.75.5009.
9. Paik, P. K. *et al.* A Phase Ib Open-Label Multicenter Study of AZD4547 in Patients with Advanced Squamous Cell Lung Cancers. *Clin. Cancer Res. Off. J. Am. Assoc. Cancer Res.* 23, 5366–5373 (2017).
10. Goyal, L. *et al.* Polyclonal Secondary *FGFR2* Mutations Drive Acquired Resistance to FGFR Inhibition in Patients with FGFR2 Fusion–Positive Cholangiocarcinoma. *Cancer Discov.* 7, 252–263 (2017).
11. Chell, V. *et al.* Tumour cell responses to new fibroblast growth factor receptor tyrosine kinase inhibitors and identification of a gatekeeper mutation in FGFR3 as a mechanism of acquired resistance. *Oncogene* 32, 3059–3070 (2013).
12. Byron, S. A. *et al.* The N550K/H mutations in FGFR2 confer differential resistance to PD173074, dovitinib, and ponatinib ATP-competitive inhibitors. *Neoplasia N. Y. N* 15, 975–988 (2013).
13. Herrera-Abreu, M. T. *et al.* Parallel RNA interference screens identify EGFR activation as an escape mechanism in FGFR3-mutant cancer. *Cancer Discov.* 3, 1058–1071 (2013).
14. Kim, S.-M. *et al.* Activation of the Met kinase confers acquired drug resistance in FGFR-targeted lung cancer therapy. *Oncogenesis* 5, e241 (2016).
15. Chang, J. *et al.* Multiple receptor tyrosine kinase activation attenuates therapeutic efficacy of the fibroblast growth factor receptor 2 inhibitor AZD4547 in FGFR2

amplified gastric cancer. *Oncotarget* 6, 2009–2022 (2015).

16. Wang, J. *et al.* Ligand-associated ERBB2/3 activation confers acquired resistance to FGFR inhibition in FGFR3-dependent cancer cells. *Oncogene* 34, 2167–2177 (2015).
17. Wilson, T. R. *et al.* Widespread potential for growth-factor-driven resistance to anticancer kinase inhibitors. *Nature* 487, 505–509 (2012).
18. Harbinski, F. *et al.* Rescue screens with secreted proteins reveal compensatory potential of receptor tyrosine kinases in driving cancer growth. *Cancer Discov.* 2, 948–959 (2012).
19. Kas, S. M. *et al.* Insertional mutagenesis identifies drivers of a novel oncogenic pathway in invasive lobular breast carcinoma. *Nat. Genet.* (2017) doi:10.1038/ng.3905.
20. Doornebal, C. W. *et al.* A preclinical mouse model of invasive lobular breast cancer metastasis. *Cancer Res.* 73, 353–363 (2013).
21. Allen, J. D., Jackson, S. C. & Schinkel, A. H. A mutation hot spot in the Bcrp1 (Abcg2) multidrug transporter in mouse cell lines selected for Doxorubicin resistance. *Cancer Res.* 62, 2294–2299 (2002).
22. van de Wetering, K. & Sapth, S. ABCG2 functions as a general phytoestrogen sulfate transporter in vivo. *FASEB J.* 26, 4014–4024 (2012).
23. van de Wetering, K. *et al.* Intestinal breast cancer resistance protein (BCRP)/Bcrp1 and multidrug resistance protein 3 (MRP3)/Mrp3 are involved in the pharmacokinetics of resveratrol. *Mol. Pharmacol.* 75, 876–885 (2009).
24. Stern, D. L. Tagmentation-Based Mapping (TagMap) of Mobile DNA Genomic Insertion Sites. (2017) doi:10.1101/037762.
25. Pettersen, E. F. *et al.* UCSF Chimera--a visualization system for exploratory research and analysis. *J. Comput. Chem.* 25, 1605–1612 (2004).
26. de Ruiter, J. R. *et al.* Identifying transposon insertions and their effects from RNA-sequencing data. *Nucleic Acids Res.* 45, 7064–7077 (2017).
27. Wu, Y.-M. *et al.* Identification of targetable FGFR gene fusions in diverse cancers. *Cancer Discov.* 3, 636–647 (2013).
28. de Ronde, J. J., Rigaill, G., Rottenberg, S., Rodenhuis, S. & Wessels, L. F. A. Identifying subgroup markers in heterogeneous populations. *Nucleic Acids Res.* 41, e200 (2013).
29. Brinkman, E. K., Chen, T., Amendola, M. & van Steensel, B. Easy quantitative assessment of genome editing by sequence trace decomposition. *Nucleic Acids Res.* 42, e168 (2014).
30. Perna, D. *et al.* BRAF inhibitor resistance mediated by the AKT pathway in an oncogenic BRAF mouse melanoma model. *Proc. Natl. Acad. Sci. U. S. A.* 112, E536–545 (2015).
31. Chapeau, E. A. *et al.* Resistance mechanisms to TP53-MDM2 inhibition identified by in vivo piggyBac transposon mutagenesis screen in an Arf(-/-) mouse model. *Proc. Natl. Acad. Sci. U. S. A.* (2017) doi:10.1073/pnas.1620262114.
32. Temiz, N. A. *et al.* RNA sequencing of Sleeping Beauty transposon-induced tumors

- p>detects transposon-RNA fusions in forward genetic cancer screens.
- Genome Res.*
- 26, 119–129 (2016).
33. Rotow, J. & Bivona, T. G. Understanding and targeting resistance mechanisms in NSCLC. *Nat. Rev. Cancer* 17, 637–658 (2017).
 34. Niederst, M. J. & Engelman, J. A. Bypass mechanisms of resistance to receptor tyrosine kinase inhibition in lung cancer. *Sci. Signal.* 6, re6 (2013).
 35. Hayashi, T. *et al.* RASA1 and NF1 are preferentially co-mutated and define a distinct genetic subset of smoking-associated non-small cell lung carcinomas sensitive to MEK inhibition. *Clin. Cancer Res. Off. J. Am. Assoc. Cancer Res.* (2017) doi:10.1158/1078-0432.CCR-17-2343.
 36. Patch, A.-M. *et al.* Whole-genome characterization of chemoresistant ovarian cancer. *Nature* 521, 489–494 (2015).
 37. Natarajan, K., Xie, Y., Baer, M. R. & Ross, D. D. Role of breast cancer resistance protein (BCRP/ABCG2) in cancer drug resistance. *Biochem. Pharmacol.* 83, 1084–1103 (2012).
 38. Tan, L. *et al.* Development of covalent inhibitors that can overcome resistance to first-generation FGFR kinase inhibitors. *Proc. Natl. Acad. Sci. U. S. A.* 111, E4869–4877 (2014).
 39. Venetsanakos, E. *et al.* The Irreversible Covalent Fibroblast Growth Factor Receptor Inhibitor PRN1371 Exhibits Sustained Inhibition of FGFR after Drug Clearance. *Mol. Cancer Ther.* 16, 2668–2676 (2017).
 40. Brunen, D. & Bernards, R. Drug therapy: Exploiting synthetic lethality to improve cancer therapy. *Nat. Rev. Clin. Oncol.* 14, 331–332 (2017).
 41. Cong, L. *et al.* Multiplex genome engineering using CRISPR/Cas systems. *Science* 339, 819–823 (2013).
 42. Harmsen, T., Klaasen, S., van de Vrugt, H. & Te Riele, H. DNA mismatch repair and oligonucleotide end-protection promote base-pair substitution distal from a CRISPR/Cas9-induced DNA break. *Nucleic Acids Res.* 46, 2945–2955 (2018).
 43. Henneman, L. *et al.* Selective resistance to the PARP inhibitor olaparib in a mouse model for BRCA1-deficient metaplastic breast cancer. *Proc. Natl. Acad. Sci.* 112, 8409–8414 (2015).
 44. Boelens, M. C. *et al.* PTEN Loss in E-Cadherin-Deficient Mouse Mammary Epithelial Cells Rescues Apoptosis and Results in Development of Classical Invasive Lobular Carcinoma. *Cell Rep.* 16, 2087–2101 (2016).
 45. Martin, M. Cutadapt removes adapter sequences from high-throughput sequencing reads. *EMBnet.journal* 17, 10 (2011).
 46. Dobin, A. *et al.* STAR: ultrafast universal RNA-seq aligner. *Bioinforma. Oxf. Engl.* 29, 15–21 (2013).
 47. Ewels, P., Magnusson, M., Lundin, S. & Käller, M. MultiQC: summarize analysis results for multiple tools and samples in a single report. *Bioinforma. Oxf. Engl.* 32, 3047–3048 (2016).
 48. Liao, Y., Smyth, G. K. & Shi, W. featureCounts: an efficient general purpose program for assigning sequence reads to genomic features. *Bioinforma. Oxf. Engl.* 30, 923–930 (2014).

49. Anders, S. & Huber, W. Differential expression analysis for sequence count data. *Genome Biol.* 11, R106 (2010).
50. Lai, Z. *et al.* VarDict: a novel and versatile variant caller for next-generation sequencing in cancer research. *Nucleic Acids Res.* 44, e108 (2016).
51. McLaren, W. *et al.* The Ensembl Variant Effect Predictor. *Genome Biol.* 17, 122 (2016).
52. Köster, J. & Rahmann, S. Snakemake--a scalable bioinformatics workflow engine. *Bioinforma. Oxf. Engl.* 28, 2520–2522 (2012).
53. Picelli, S. *et al.* Tn5 transposase and tagmentation procedures for massively scaled sequencing projects. *Genome Res.* 24, 2033–2040 (2014).
54. Langmead, B. & Salzberg, S. L. Fast gapped-read alignment with Bowtie 2. *Nat. Methods* 9, 357–359 (2012).
55. de Jong, J. *et al.* Computational identification of insertional mutagenesis targets for cancer gene discovery. *Nucleic Acids Res.* 39, e105 (2011).
56. de Ruiter, J. R. *et al.* Identifying transposon insertions and their effects from RNA-sequencing data. *Nucleic Acids Res.* 45, 7064–7077 (2017).

